

Causal Drivers of Land-Atmosphere Carbon Fluxes from Machine Learning Models and Data

Mozhgan A. Farahani¹, Allison E. Goodwell^{1,2}

¹University of Colorado Denver, Department of Civil Engineering

²Prairie Research Institute, University of Illinois at Urbana-Champaign

²Prairie Research Institute, 615 E. Peabody Dr. MC-650, Champaign, IL 61820

Key Points:

- Information theory measures describe individual and joint causal relationships in observed versus modeled vertical carbon dioxide fluxes.
- Three machine learning models overestimate unique information from sources at the expense of synergistic, or pairwise information.
- Regionally trained models have improved functional performance that is not always captured by traditional predictive performance metrics.

Corresponding author: Allison Goodwell, goodwe12@illinois.edu

14 Abstract

15 Interactions among atmospheric, root-soil, and vegetation processes drive carbon
 16 dioxide fluxes (F_c) from land to atmosphere. Eddy covariance measurements are com-
 17 monly used to measure F_c at sub-daily timescales and validate process-based and data-
 18 driven models. However, these validations do not reveal process interactions, thresholds,
 19 and key differences in how models replicate them. We use information theory-based mea-
 20 sures to explore multivariate information flow pathways from forcing data to observed
 21 and modeled hourly F_c , using flux tower datasets in the Midwestern U.S. in intensively
 22 managed corn-soybean landscapes. We compare Multiple Linear Regressions (MLR), Long-
 23 Short Term Memory (LSTM), and Random Forests (RF) to evaluate how different model
 24 structures use information from combinations of sources to predict F_c . We extend a frame-
 25 work for model predictive performance and functional performance, which examines the
 26 full suite of dependencies from all forcing variables to the observed or modeled target.
 27 Of the three model types, RF exhibited the highest functional and predictive performance.
 28 Regionally trained models demonstrate lower predictive but higher functional performance
 29 compared to site-specific models, suggesting superior reproduction of observed relation-
 30 ships. This study shows that some metrics of predictive performance encapsulate func-
 31 tional behaviors better than others, highlighting the need for multiple metrics of both
 32 types. This study improves our understanding of carbon fluxes in an intensively man-
 33 aged landscape, and more generally provides insight into how model structures and forc-
 34 ing variables translate to interactions that are well versus poorly captured in models.

35 Plain Language Summary

36 In an agricultural landscape, exchanges of carbon dioxide between the land and at-
 37 mosphere occur due to photosynthesis and respiration, and depend on weather, soil, and
 38 vegetation conditions. In modeling, predictive performance focuses on the relationship
 39 between observed and modeled outputs, while functional performance considers the re-
 40 lationships between interacting inputs and outputs. We compare several performance
 41 measures for three different machine learning models that simulate sub-daily carbon fluxes.
 42 We look at how drivers such as solar radiation, soil moisture, temperature, humidity, and
 43 rainfall provide information to carbon fluxes, and whether different machine learning mod-
 44 els also capture these interactions. In other words:

45 *Air, soil, and plants drive carbon's upward path,*
 46 *Models are detectives, interpreting their math.*
 47 *With information theory, we map data's travel courses,*
 48 *To see how models find or miss carbon's causal sources.*

49 1 Introduction

50 The ecohydrologic system constitutes a complex web of interactions between wa-
 51 ter, soil, and vegetation. The exchange of carbon dioxide (CO_2) between the land and
 52 atmosphere plays a significant role in the Earth's surface temperature balance, and is
 53 one of these key process affected by hydrological and ecological feedback (Liang et al.,
 54 2020). In terrestrial ecosystems, the carbon exchange rate is mainly controlled by the
 55 photosynthesis - respiration process. Complex and nonlinear drivers such as meteorol-
 56 ogy, soils, vegetation, and available energy cause vertical carbon fluxes to be highly vari-
 57 able in space and time and challenging to measure and model (Huang et al., 2017; He
 58 et al., 2018; Chen et al., 2020; Dou & Yang, 2018). Several approaches have been devel-
 59 oped to understand current and future terrestrial carbon flux over the past several decades
 60 involving field observations (Falge et al., 2002; Xiao et al., 2011), large-scale remote sens-
 61 ing (Xiao et al., 2019), process-based modeling (D. Wang et al., 2011; Dunkl et al., 2021),
 62 or a combination of these methods (Vetter et al., 2008; Jung et al., 2011). We take a data-

63 driven approach to explore the predictability of the net CO_2 exchange rate, also known
64 as Net Ecosystem CO_2 exchange (NEE), in agricultural landscapes in the Midwest U.S.
65 NEE is the net carbon balance between photosynthetic CO_2 gain and respiratory CO_2
66 losses from plants and animals, and we use F_c as the nomenclature for NEE measured
67 at an eddy covariance flux tower.

68 In this system, causal interactions need to be detected to understand interrelated
69 processes at multiple spatial and temporal scales (Runge et al., 2019; Bollt et al., 2018).
70 From a modeling perspective, this involves “intervening” in the system and manipulating
71 model structures, parameters, or inputs, and observing the resulting model behavior
72 relative to observations (Goodwell et al., 2020). Specifically, a causal model evaluation
73 framework should consider dependencies between inputs or source variables and
74 the target, or the “functional performance” relative to observed interactions (Goodwell
75 & Bassiouni, 2022; Bassiouni & Vico, 2021; Ruddell et al., 2019). This is particularly crucial
76 for machine learning and deep learning models, where relationships between inputs
77 and outputs are not transparent. Understanding how these models learn, or fail to learn,
78 the dependencies we observe in nature to predict an output is vital (Goodfellow et al.,
79 2016). Meanwhile, predictive performance measures capture features of the relationship
80 between the observed and modeled target output variable. In this study, we focus on the
81 functional and predictive performance of data-driven models of hourly F_c .

82 Information theory (IT) measures, which characterize uncertainty and reductions
83 in uncertainty based on probability distributions (Cover & Thomas, 2012; Shannon, 1948),
84 have been employed in various geoscience contexts to measure complexity, dependencies,
85 and driving or causal mechanisms (Balasis et al., 2013). Previous applications character-
86 ized ecohydrological process networks that reveal ecosystem behaviors (Ruddell & Kumar,
87 2009a; Franzen et al., 2020; Goodwell & Kumar, 2017; Ruddell et al., 2019; Sendrowski
88 & Passalacqua, 2017). Recent applications of IT-based measures in hypothesis testing
89 frameworks (Nearing et al., 2016, 2018) and to evaluate the functional performance of
90 models based on a selection of sources (Sendrowski et al., 2018; Ruddell et al., 2019; Ten-
91 nant et al., 2020; Moges et al., 2022; Bassiouni & Vico, 2021; Goodwell & Bassiouni, 2022)
92 have shown great potential to better understand how models capture causal interactions
93 in various Earth systems. However, these studies tend to consider a small subset of sources
94 or a single modeled process. In this study, we take a more comprehensive view of complex
95 ecohydrologic models and analyze information flow through the entire model. This
96 allows for identification of potential sources of model error and insights into the relation-
97 ships between different components of the model. This can lead to a better understand-
98 ing of the model’s behavior and performance, and ultimately, more accurate predictions
99 of ecological and hydrological processes.

100 ML techniques have shown to be more effective and adaptable relative to mecha-
101 nistic or semi-empirical model approaches, providing a complementary strategy to pre-
102 dict carbon fluxes at local to global scales (Dou & Yang, 2018; Dou et al., 2018). Ma-
103 chine learning (ML) algorithms construct empirical models based on the patterns con-
104 tained in data and are very data adaptive because no assumption and functional forms
105 need to be prescribed (Jung et al., 2011). ML has been used for interpolation for gap-
106 filling carbon flux data and climatic driving factors based on flux tower measurements
107 (Moffat et al., 2007; Ooba et al., 2006), decreasing the predictive errors of carbon fluxes
108 from the land surface models (T. Wang et al., 2012), and upscaling carbon fluxes of ter-
109 restrial ecosystems from site to regional and global scales (Papale et al., 2015). Several
110 studies similarly indicate the ability of ML to reproduce complex ecohydrological pat-
111 terns, particularly in relation to flux tower measurements (Q. Zhou et al., 2019; Tramon-
112 tana et al., 2020; Reichstein et al., 2019). Specifically, Q. Zhou et al. applied a ML ap-
113 proach to estimate NEE using variables such as the fraction of photosynthetically active
114 radiation (PAR), leaf area index (LAI), soil moisture, downward solar radiation, precip-
115 itation, and mean air temperature. Tramontana et al. developed an ANN model to es-

116 timate NEE based on the light-use efficiency concept and used a comprehensive dataset
117 of soil and micrometeorological variables as flux drivers.

118 While machine learning models tend to make better predictions than traditional
119 models, they are often not trusted by the hydrologic community due to their black-box
120 nature (Welchowski et al., 2022). By characterizing information flow pathways and com-
121 paring models beyond predictive performance, we can gain insights into their process rep-
122 resentations (Goodwell & Bassiouni, 2022). This is particularly important when using
123 a certain model to extrapolate in an unknown future climate, where a model with bet-
124 ter process representations may be more trustworthy to apply to an unseen scenario. In
125 this paper, we apply our IT-based model evaluation framework to three ML models, Long
126 Short Term Memory (LSTM), Random Forest (RF), and multiple linear regression (MLR)
127 to characterize how these models reproduce observed dependencies in terms of individ-
128 ual, pairwise and more multivariate interactions to predict sub-daily F_c . Recurrent Neu-
129 ral Networks (RNN) with LSTM are deep learning models that can successfully learn
130 long-range temporal dependencies between time steps of sequence data (Hochreiter &
131 Schmidhuber, 1997a; Sutskever et al., 2014; Kratzert et al., 2018, 2019). Meanwhile, the
132 RF is a classical ML method that is known for its capacity to handle large datasets, re-
133 sist the negative impacts of noise and overfitting (Breiman, 2001), and rank the signif-
134 icance of input variables (Leroux et al., 2017; Meng et al., 2021). RFs have been exten-
135 sively applied in ecological classification and regression tasks (Meyer et al., 2019; Reitz
136 et al., 2021; Q. Zhou et al., 2019). We use MLR as a simple model with which to com-
137 pare the more complex ML models. We develop both locally and regionally trained mod-
138 els to compare model responses to larger training datasets that span multiple sites.

139 This paper is organized as follows. Section 2 describes the study site, datasets used,
140 machine learning model development, and model evaluation. Section 3 presents the re-
141 sults of MLR, RF, and LSTM models. Section 4 provides a discussion, and Section 5 is
142 a conclusion.

143 2 Materials and Methods

144 2.1 Site Description and Data

145 The data for this study was collected from multiple flux tower sites in maize/soybean
146 landscapes in the Upper Midwest Corn Belt. The Goose Creek flux tower in central Illi-
147 nois (Figure 1a) is part of the NSF-funded Critical Interface Network (CINet) project
148 (<https://cinet.ncsa.illinois.edu/>), and collects 15-minute fluxes and meteorolog-
149 ical variables at a 25m height, along with vegetation and soil properties. The Goose Creek
150 site has been extensively studied using Lidar topography and high-resolution modeling
151 of nutrient and carbon fluxes (Yan et al., 2019; Dutta et al., 2017; Woo & Kumar, 2017),
152 and footprint modeling has been applied to study how landscape heterogeneity influences
153 evapotranspiration fluxes (Hernandez Rodriguez et al., 2023). For this study, the 15-minute
154 data was resampled to hourly resolution to match with other sites.

155 We also use data from 5 maize-soybean rotation sites in the FLUXNET2015 (Pastorello
156 et al., 2020) dataset (Table 1), which provides over 1500 site-years of quality-controlled
157 datasets for various landscapes. We used the AmeriFlux version of the hourly carbon
158 flux data and meteorological variables for sites US-Ne1 (Mead - irrigated continuous maize
159 site), US-Ne2 (Mead - irrigated maize-soybean rotation site), and US-Ne3 (Mead - rain-
160 fed maize-soybean rotation site). These sites are located within 1.6 km of each other at
161 the University of Nebraska Agricultural Research and Development Center near Mead,
162 Nebraska. Additionally, we used the hourly measurements of sites US-Br1 and US-Br3,
163 located in adjacent maize and soybean fields in central Iowa. The farming systems, as-
164 sociated tillage, and nutrient management practices for maize/soybean production at these
165 sites are typical of those throughout the Upper Midwest Corn Belt.

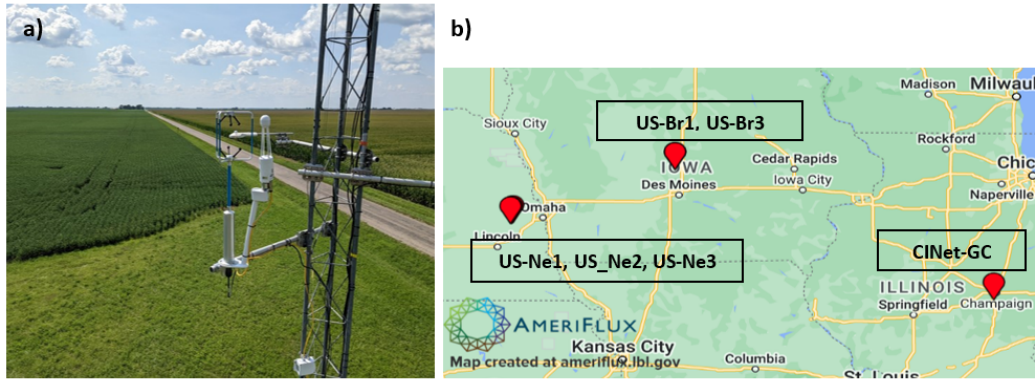


Figure 1: (a) At a 25m height eddy covariance flux tower in Central Illinois, observed fluxes originate from up to a 10km surrounding region, dominated by a patchwork of maize and soybean fields. (b) Three flux tower sites are located in maize/soybean systems.

Table 1: Characteristics of flux tower sites. MAT, ($^{\circ}C$) is Mean Annual Temperature. MAP (mm) is Mean Annual Precipitation.

Site ID	Name	MAT	MAP	Year	Reference
US-Ne1	Mead-irrigated continuous maize	10.07	790.37	2010-2021	(Suyker, 2022a)
US-Ne2	Mead-irrigated maize-soybean rotation	10.08	788.89	2010-2021	(Suyker, 2022b)
US-Ne3	Mead-rainfed maize-soybean rotation	10.11	783.68	2010-2021	(Suyker, 2022c)
US-Br1	Brooks Field Site 10-Ames	8.95	842.33	2005-2011	(Prueger & Parkin, 2016a)
US-Br3	Brooks Field Site 11-Ames	8.9	846.6	2005-2011	(Prueger & Parkin, 2016b)
CINet-GC	Goose Creek flux tower	10	900	2016-2020	(Hernandez Rodriguez et al., 2023)

166 The forcing variables selected for this study (Table 2) are expected to influence the
 167 dynamics of F_c between the land and atmosphere, through direct or indirect influence
 168 on photosynthesis, respiration, and other biogeochemical processes. Specifically:

- 169 • T_a and T_S : Soil and air temperatures influence both photosynthetic rates and mi-
 170 crobial respiration. For example, it has been found that plant respiration increases
 171 more than photosynthesis as temperature rises, which indicates that a substan-
 172 tial temperature increase could turn an ecosystem from a carbon source to a sink
 173 (X. Zhou et al., 2012). Meanwhile, other studies have determined that this rela-
 174 tionship is more complex when aspects such as changing rainfall and atmospheric
 175 CO_2 concentrations are considered (Drewry et al., 2010a, 2010b; Le et al., 2011).

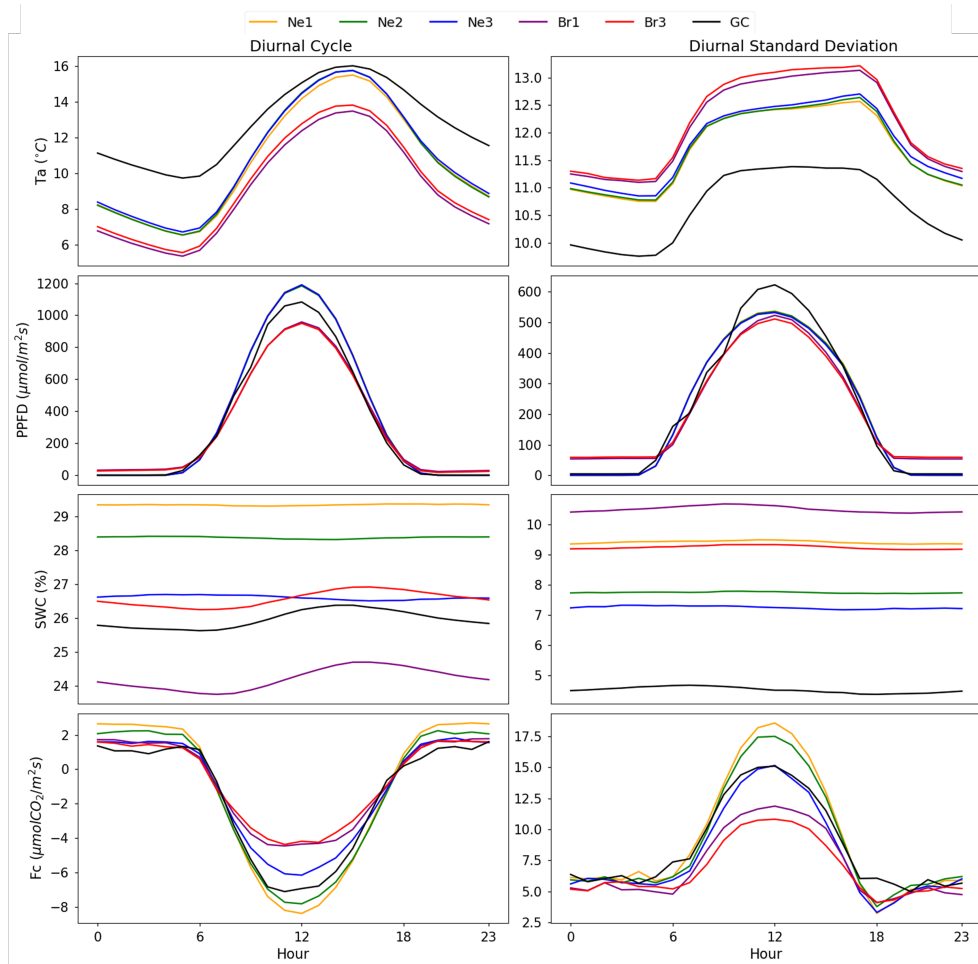


Figure 2: Diurnal cycle (left panel) and diurnal standard deviation cycle (right panel) of air temperature (T_a), photosynthetic photon flux density ($PPFD$), soil water content (SWC) and carbon flux (F_c) over the study years corresponded to different sites (Ne1, Ne2, Ne3, Br1, Br3, GC). Each site is represented by a unique color.

Table 2: The full suite of variables used in this study.

Variable Description	Symbol	Unit
Carbon dioxide (CO_2) flux	Fc	$\mu mol CO_2 / m^2 s$
Relative humidity	RH	%
Air temperature	Ta	$^{\circ}C$
Wind speed	WS	m/s
Atmospheric pressure	Pa	kPa
Precipitation	P	mm
Net radiation	$NETRAD$	W/m^2
Incoming photosynthetic photon flux density	$PPFD$ *	$\mu mol Photons / m^2 s$
Soil water content (volumetric)	SWC	%
Soil temperature	TS	$^{\circ}C$

* PAR: Photosynthetically Active Radiation ($\mu mol / m^2 s$) in the CINet-GC site

- 176 • RH : Humidity levels can impact plant transpiration and stomatal conductance,
177 thereby influencing carbon uptake during photosynthesis.
178 • P and SWC : Water availability affects photosynthesis, and scarcity can lead to
179 stress conditions, slowing down carbon sequestration.
180 • $PPFD$ and $NETRAD$: These radiation variables influence the energy balance and
181 are related to the amount of light available for photosynthesis, which is a primary
182 driver for carbon uptake in plants.
183 • WS : While not a direct factor, wind speed can affect plant transpiration rates, hu-
184 midity levels, and even the mixing of carbon dioxide in the atmospheric layer.
185 • Pa : Changes in atmospheric pressure can impact gas exchange rates, indirectly
186 affecting Fc .

187 We undertook rigorous data pre-processing (SI section S1) to ensure the reliabil-
188 ity of our analysis. This involved applying quality control measures to all datasets, and
189 identifying and removing any outliers or erroneous patterns. We encountered missing val-
190 ues in some datasets, which we imputed using time series imputation methods. We note
191 that imputation is based on certain assumptions and can introduce uncertainty, which
192 is discussed along with the results.

193 2.2 Model Development and Experimental Design

194 In this study, we develop three ML models to predict Fc : Multiple Linear Regres-
195 sion (MLR), Long Short Term Memory (LSTM), and Random Forest (RF). Each of these
196 models offers unique advantages and capabilities. To ensure efficient learning, all input
197 driving variables and the output (Fc) data were normalized by subtracting the mean and
198 dividing by the standard deviation (Minns & Hall, 1996). The output of all ML mod-
199 els was retransformed using the normalization parameters to obtain the final Fc predic-
200 tion.

201 The setup of ML models necessitates the optimization of hyperparameters, a task
 202 we performed via a combination of grid search and cross-validation techniques. Grid search
 203 encompasses defining a range of possible parameter values and evaluating the model’s
 204 performance for each combination. Cross-validation helps to evaluate the model’s gen-
 205 eralization ability by partitioning the data into training and validation sets. We used a
 206 5-fold cross-validation approach to search over the hyperparameter grid, where the data
 207 were split into 5 subsets of equal size, and each subset was used once for validation while
 208 the remaining 4 subsets were used for training. This process was repeated multiple times
 209 with different partitions to ensure a robust estimate of the model’s performance.

210 The ML architectures (refer to SI, Table S1) used in this study worked well for all
 211 sites in comparison to observation and were therefore chosen to be applied here without
 212 further tuning. However, a systematic sensitivity analysis of the effects of different hy-
 213 perparameters was not performed in our study and could be explored in more detail in
 214 terms of their effect on predictive and functional performance.

215 ***2.2.1 Multiple Linear Regression Model***

216 MLR assumes a linear function of the independent variables to predict the depend-
 217 ent variable. The simplicity, interpretability, and ease of use of MLR make it a popu-
 218 lar choice for many applications. However, it assumes a linear relationship between the
 219 dependent and independent variables and is sensitive to outliers and multicollinearity.
 220 In our study, MLR provides a baseline for comparison with the more complex RF and
 221 LSTM models. We adopted the Ordinary Least Squares (OLS) method for model fitting,
 222 which optimizes the model by minimizing the sum of the squared residuals.

223 ***2.2.2 Random Forest Model***

224 The Random Forest (RF) model is a powerful ensemble learning algorithm that gen-
 225 erates predictions by combining the outputs of multiple decision trees. Each of these trees
 226 is constructed using a randomly selected subset of the features and data samples, which
 227 helps to prevent overfitting. The final prediction is then derived by averaging the out-
 228 puts from all the trees. In a decision tree, each node represents a feature in our data, each
 229 branch represents a decision rule, and each leaf represents an outcome. The root node,
 230 the topmost node in a tree, corresponds to the best predictor. Decisions are made by walk-
 231 ing down the tree from the root to a leaf node.

232 The RF model is highly regarded for its accuracy, resilience to noise and outliers,
 233 and its ability to handle high-dimensional data with nonlinear relationships and miss-
 234 ing values (Breiman, 2001), making it a suitable choice for our study to predict Fc . How-
 235 ever, due to its complexity, interpreting the model can be challenging, and the compu-
 236 tational cost can increase significantly with the number of trees in the forest. The per-
 237 formance of the RF model is significantly influenced by the fine-tuning of hyperparam-
 238 eters. The n -estimators (set to 100 in this study) parameter represents the number of
 239 trees in the forest and a trade-off between computation time and model performance. The
 240 max-depth parameter (set to 9, total number of features) controls the complexity of the
 241 model, playing a crucial role in preventing overfitting. The max-features parameter (set
 242 to 3), denoting the number of features to consider at each split (the maximum depth of
 243 each tree), can significantly impact the model’s performance and is typically set to the
 244 square root of the total number of features. It is also worth noting that the random-state
 245 (set to 42) parameter ensures the consistency and reproducibility of our results.

246 ***2.2.3 Long Short Term Memory Model***

247 LSTM is a specialized form of the Artificial Recurrent Neural Network (RNN) ar-
 248 chitecture, which is designed to remember long-term dependencies in sequential data. This

249 capability is achieved through a unique arrangement of memory cells and three types of
 250 gates: the input gate, output gate, and forget gate. These components work together to
 251 selectively retain or discard information over time, making LSTM particularly adept at
 252 time-series prediction tasks (Hochreiter & Schmidhuber, 1997b). We choose LSTM for
 253 its capacity to model temporal dependencies in time series data, a vital characteristic
 254 for accurate carbon flux prediction. We operate the LSTM in sequence-to-sequence mode,
 255 in which any length of input sequence generates an equally long output sequence. We
 256 chose a constant sequence length of 12 hourly time steps. This is based on the diurnal
 257 cycle of environmental patterns, including temperature and light, that significantly affect
 258 F_c (Figure 2).

259 The design and training of LSTM models necessitate careful selection of various
 260 parameters. These include the number of layers in the network, the number of hidden
 261 units per layer, the learning rate, and the sensitivity of back-propagation to residuals be-
 262 tween predicted and observed outputs. Additionally, the presence or absence of dropout
 263 layers, which help prevent overfitting, must be considered. To find an optimal model ar-
 264 chitecture, we conducted a series of experiments at different sites, manually adjusting
 265 different architectures (e.g., one or two LSTM layers or 5, 10, 15, or 20 cell/hidden units).
 266 The chosen architecture consists of a two-layer LSTM network, with each layer having
 267 a cell/hidden state length of 9, as number of driving source variables (Table 2). Dropout
 268 layers are added between the LSTM layers to prevent overfitting (Srivastava et al., 2014),
 269 and a regression layer with a single unit is added for the target variable (F_c).

270 During the training of LSTMs, each iteration step typically works with a subset
 271 (called a batch or mini-batch) of the available training data. In our case, the batch size
 272 is defined to be 128, and each sample in the batch consists of the F_c value and the driv-
 273 ing variables of the 12 preceding time steps. The loss function, calculated as the average
 274 of the Mean Squared Error (MSE) of simulated and observed F_c of these 128 sam-
 275 ples, is computed in every iteration step. For faster convergence, it is advantageous to
 276 have random samples in one batch. In traditional ecohydrological model calibration, the
 277 number of iteration steps defines the total number of model runs performed during cali-
 278 bration. The corresponding term for neural networks is called an “epoch”, which is de-
 279 fined as the period in which each training sample is used once for updating the model
 280 parameters. For instance, if the dataset consists of 1000 training samples and the batch
 281 size is 10, one epoch would consist of 100 iteration steps.

282 **2.2.4 Experimental Setup**

283 Our experimental design involves two main experiments aimed at evaluating the
 284 performance of our ML models in predicting F_c .

285 **Local models for each site:** This experiment tests the general ability of our MLMs
 286 to predict F_c at individual sites. We trained separate models for each site (Table 1) us-
 287 ing the first 80% of the studied years as training data and the last 20% of studied years
 288 as the testing period. This resulted in six separately trained networks, one for each site.

289 **Regional model:** We train a regional model on a large dataset with data from all sites,
 290 to learn general patterns and relationships between input and output data. In this, we
 291 grouped all sites for the definition of the study region and used the combined data of 80%
 292 randomly selected for the entire period of all sites. We then test the model on each of
 293 the sites separately. The regional experiment is motivated by the idea that deep learn-
 294 ing models perform better when trained with large amounts of data (Hestness et al., 2017;
 295 Schmidhuber, 2015) and regional models could be a potential solution for prediction in
 296 sites without flux tower measurements (Hrachowitz et al., 2013; Sivapalan, 2003). Hav-
 297 ing a large training dataset allows the model to learn more generalized and abstract pat-
 298 terns and relationships between input and output data. For instance, if two sites behave
 299 similarly, but one lacks high precipitation events or extended drought periods in the cal-

300 ibration period, while having these events in the validation period, the ML model can
 301 learn the response behavior to those extremes and use this knowledge in the first site.

302 **2.3 Model Evaluation Framework**

303 We gauge model performance both in terms of predictive accuracy and ability to
 304 encapsulate functional relationships. In this context, we consider two types of performance
 305 measures: predictive performance, which assesses the model’s ability to accurately pre-
 306 dict outcomes, and functional performance, which evaluates the model’s ability to cap-
 307 ture the underlying functional relationships between variables (Nearing et al., 2020; Good-
 308 well & Bassiouni, 2022; Bassiouni & Vico, 2021). Predictive performance metrics include
 309 quantitative measures of the discrepancy between the model’s predictions and the actual
 310 values, while functional performance can be assessed using various methods, including
 311 sensitivity analysis, partial dependence plots, and information-theoretic measures. We
 312 use a combination of several predictive and functional performance measures to evalu-
 313 ate the performance of ML models at different granularities.

314 **2.3.1 Predictive Performance**

315 We use Nash–Sutcliffe Efficiency (*NSE*) (Nash & Sutcliffe, 1970), Kling-Gupta Ef-
 316 ficiency (*KGE*) (Gupta et al., 2009), and Shannon Entropy (*H*) (Shannon, 1948), an information
 317 theory (IT)-based measure to evaluate model predictive performance. Both *NSE* and
 318 *KGE* are widely recognized in hydrology for their effectiveness in assessing the quality
 319 of modeled predictions in relation to observed data. On the other hand, the entropy met-
 320 ric quantifies the uncertainty inherent in the model’s predictions relative to observations.
 321 These metrics provide different perspectives on prediction errors.

322 The *NSE* is a normalized statistic that quantifies the relative magnitude of the resid-
 323 ual variance, often referred to as “noise”, in comparison to the variance of the measured
 324 data, or “information” (Nash & Sutcliffe, 1970). It is computed as follows:

$$\text{NSE}(y, \hat{y}) = 1 - \frac{\sum_{i=1}^n (y_i - \hat{y}_i)^2}{\sum_{i=1}^n (y_i - \bar{y})^2} \quad (1)$$

325 where n is the number of observations, \bar{y} is the mean of modeled values and y_i and \hat{y}_i
 326 are the observed and modeled values, respectively. The *NSE* ranges from $-\infty$ to 1. An
 327 *NSE* of 1 signifies a perfect match between modeled and observed data. An *NSE* of 0
 328 indicates that the model’s predictions are as accurate as the mean of the observed data.
 329 A negative *NSE* occurs when the observed mean is a better predictor than the model.

330 The *KGE* is defined by the following equation:

$$\text{KGE}(y, \hat{y}) = 1 - \sqrt{(r(y, \hat{y}) - 1)^2 + (\alpha(y, \hat{y}) - 1)^2 + (\beta(y, \hat{y}) - 1)^2}, \quad (2)$$

331 where r is the Pearson correlation coefficient between the observed (y_i) and modeled val-
 332 ues (\hat{y}_i), defined as:

$$r(y, \hat{y}) = \frac{\sum_{i=1}^n (y_i - \bar{y})(\hat{y}_i - \bar{\hat{y}})}{\sqrt{\sum_{i=1}^n (y_i - \bar{y})^2 (\hat{y}_i - \bar{\hat{y}})^2}} \quad (3)$$

333 Here, n is the number of observations, and \bar{y} and $\bar{\hat{y}}$ are the mean of observed and mod-
 334 eled values, respectively. The variability ratio, α , is the ratio of the standard deviation
 335 of modeled values ($\sigma_{\hat{y}}$) to observed values (σ_y). β , the bias ratio, is the ratio of the mean

336 of modeled values (\bar{y}) to observed values (\bar{y}). Similar to NSE, *KGE* values range between
 337 $-\infty$ and 1, where 1 represents a perfect fit.

338 The *NSE* and *KGE* can be more or less suitable depending on the characteristics
 339 of the data and the objectives of the model (Knoben et al., 2019). *NSE* is based on the
 340 mean squared error and is particularly sensitive to the ability of the model to reproduce
 341 the variance of the data around its mean. Consequently, a model's consistent over- or
 342 underestimation can influence the *NSE* value. If the model consistently over- or under-
 343 estimates the data, this will strongly affect the *NSE*. On the other hand, *KGE* also in-
 344 cludes the correlation between observed and simulated data in addition to bias and vari-
 345 ability. This enables *KGE* to adeptly identify patterns of over- or underestimation. More-
 346 over, the breakdown of the *KGE* into its components can provide valuable insights into
 347 the model's strengths and weaknesses. A model might have a high *KGE*, but a low *NSE*
 348 if it reproduces the overall dynamics of the data (which *KGE* assesses) well but fails to
 349 capture the variance around the mean (which *NSE* emphasizes) accurately. Conversely,
 350 a model might have a high *NSE*, indicating a good reproduction of the observed data's
 351 variance, but a low *KGE* if there are biases or variability issues.

352 IT is based on Shannon Entropy (Shannon, 1948), $H(X) = -\sum p(x) \log_2 p(x)$,
 353 where $p(x)$ is a probability distribution function (*pdf*). $H(X)$ is a measure of uncertainty
 354 of the random variable X , or the missing information that would lead to its full predictabil-
 355 ity. Here we consider the normalized difference in entropy between observed and mod-
 356 eled *Fc* as another predictive performance measure:

$$A_H = 1 - \frac{H(Fc_{mod})}{H(Fc_{obs})} \quad (4)$$

357 A_H indicates how well the model captures the uncertainty that exists in the observed
 358 *Fc* and it ranges from $-\infty$ to 1. The values of $A_H = -\infty$ never occurs in this case
 359 as $H(Fc_{obs}) \neq 0$. $A_H = 0$ represents the "best" performance where the model ex-
 360 actly replicates the observed uncertainty. Positive values of A_H indicate that the mod-
 361 eled entropy ($H(Fc_{mod})$) is lower than the observed entropy ($H(Fc_{obs})$). In other words,
 362 the model output is less uncertain, or more predictable, than the observed data. Con-
 363 versely, negative values of A_H indicate that the model's outputs are more uncertain than
 364 the observed data. To compute *pdfs*, we discretize observed and modeled variables in
 365 $N = 100$ equally sized bins spanning the minimum and maximum values of observed
 366 output data.

367 **2.3.2 Functional Performance**

368 We also use IT to quantify the information shared between forcing variables, model
 369 outputs, and observations, which can be interpreted as a measure of the model's func-
 370 tional performance (Nearing et al., 2020). This perspective shifts the focus from uncer-
 371 tainty quantification to information quantification. We explore how various model types
 372 use information from driving variables (Table 2) to predict an output, or "target" vari-
 373 able, which here is *Fc*. The functional performance of a model indicates the extent to
 374 which this information use is similar to or different from observed dependencies. We take
 375 a multi-level IT-based approach to evaluate the functional performance of our models.
 376 We will characterize complex process linkages between forcing variables or other avail-
 377 able information sources and *Fc* to assess the model's ability in capturing the relation-
 378 ships between the driving variables and the target variable. We consider functional per-
 379 formance at several different levels, specifically for individual source-target relationships,
 380 pairs of sources, and all combinations of sources, or the whole model level.

381 For an individual source (X , here a forcing variable), and target (Y , here Fc), we
 382 consider reductions in uncertainty, or gains in information, in the form of mutual information
 383 as follows:

$$I(X; Y) = \sum p(x, y) \log_2 \left(\frac{p(x, y)}{p(x)p(y)} \right) = H(X) - H(X|Y) \quad (5)$$

384 where $I(X; Y)$ measures the reduction in uncertainty Y given the knowledge of X with
 385 units of bits. $I(X; Y)$ is symmetric with respect to X and Y , and for independent vari-
 386 ables, $I(X; Y) = 0$, while for fully dependent variables, $I(X; Y) = \min[H(X), H(Y)]$.
 387 In other words, mutual information is upper bounded by the minimum uncertainty of
 388 variables involved. We calculate functional performance for individual sources based on
 389 mutual information as follows:

$$I_n(X; Z) = \frac{I(X; Z)}{H(Z)} \quad (6)$$

$$A_{f,MI} = 1 - \frac{I_n(X; Fc_{mod})}{I_n(X; Fc_{obs})}$$

390 where $I_n(X; Y)$ is the normalized MI, $H(Z)$ is the the entropy of the target variable (Fc),
 391 $I_n(X; Fc_{obs})$ and $I_n(X; Fc_{mod})$ are normalized MI of observed and modeled target vari-
 392 able (Fc) respectively. This captures the extent to which modeled mutual information
 393 matches that of the observed target variable. $A_{f,MI}$ value close to zero represents the
 394 “best” performance where the model most closely replicates the observed mutual information.
 395 This can be used to assess how a model may be overestimating (negative $A_{f,MI}$ value)
 396 or underestimating (positive $A_{f,MI}$ value) the influence of certain drivers, and identify
 397 the most important drivers to include in a model.

398 In a more multivariate context, transfer entropy (TE) and partial information de-
 399 composition (PID) have been used to characterize interactions at different scales (Goodwell
 400 et al., 2020). TE (Schreiber, 2000) is a specific instance of conditional mutual information,
 401 which quantifies the information transferred to a target, Y_t , from a sequence of histor-
 402 ical states of another variable, given the knowledge of its own past states. In hydrologic
 403 modeling research, TE has been used to validate and diagnose missing process connec-
 404 tions in a delta model (Sendrowski et al., 2018), evaluate a multi-hypothesis ecohydro-
 405 logical modeling framework (Bennett et al., 2019), select time aggregations and lags to-
 406 ward ML applications (Tennant et al., 2020), and characterize the functional performance
 407 of a multi-layer canopy model (Ruddell et al., 2019). However, a TE-based analysis only
 408 highlights pairwise causal connections and does not address the feature of joint or simul-
 409 taneous forcing from multiple drivers. Instead, we use PID to to characterize joint in-
 410 fluences from multiple source variables to a target (Williams & Beer, 2010; Goodwell et
 411 al., 2020). For example, previous studies have compared how stomatal optimization mod-
 412 els respond to soil water supply and atmospheric demand (Bassiouni & Vico, 2021), how
 413 simple to complex models behave under different source dependencies (Goodwell & Bassiouni,
 414 2022), and stomatal model representations of physiological limits on transpiration (Hawkins
 415 et al., 2022). We consider two sources, or model forcing variables, that provide information
 416 to a target variable, which could be an observation or a model output. In a system where
 417 two sources share information from X and Y with a target Z , the total information quan-
 418 tity, $I(X, Y; Z)$, can be partitioned into synergistic (S), unique (U), and redundant (R)
 419 components. This partitioning is as follows:

$$I(X, Y; Z) = S_{X,Y} + R_{X,Y} + U_{X|Y} + U_{Y|X} \quad (7)$$

420 Here, $S_{X,Y}$ is synergistic information or joint information that is provided only when both
 421 sources are known together. $R_{X,Y}$ is redundant information or overlapping information
 422 that both sources provide individually. $U_{X|Y}$ and $U_{Y|X}$ terms indicate unique information
 423 that individuals influence when one source provides information that is not provided by
 424 the other. We use a partitioning method described in Goodwell and Kumar to obtain
 425 these components of the total information (refer to SI section S2 for more details). We
 426 normalize components by dividing each by the total mutual information $I(X, Y; Z)$, such
 427 that all information components add up to 1, and a given component indicates the frac-
 428 tion of reduced uncertainty in Z that can be attributed to that information type. These
 429 IT-based measures R , U , and S characterize different types of causal relationships be-
 430 tween variables. They are particularly useful to interpret multivariate interactions, such
 431 as the F_c -related processes of interest here.

432 For computing mutual information and information partitioning components, we
 433 used different number of bins, based on the range of observed and modeled data (i.e., the
 434 difference between the maximum and minimum values). We calculated the number of
 435 bins for the model by taking the ratio of the range of the model to the range of the ob-
 436 servation, multiplied by the number of bins in the observations ($N = 100$). This method
 437 effectively scales the number of bins based on the relative range of the model and observed
 438 data, with the assumption that a wider range would need more bins to capture the data
 439 distribution effectively. We compute statistical significance of observed or modeled IT
 440 measures using a shuffled surrogates approach (Ruddell & Kumar, 2009b). Details on
 441 these methods are provided in SI, Section S3.

442 We use PID to calculate the pairwise functional performance in terms of redundancy,
 443 synergy, and unique information and “overall” information partitioning for a given pair
 444 of sources. We consider the pairwise functional performance as the relative difference in
 445 an information flow measure for modeled versus observed data, separated into different
 446 components related to information partitioning measures S , R , and U , (Equation 7), re-
 447 spectively as $A_{f,S}$, $A_{f,R}$, and $A_{f,U}$ (Goodwell & Bassiouni, 2022). For example:

$$A_{f,S_{i,j}} = S(X_i, X_j; Z_{mod}) - S(X_i, X_j; Z_{obs}); \quad \text{for } i \neq j \quad (8)$$

448 where X_i and X_j indicate two source variables. The same concept applies for R . For unique
 449 information, we consider the sum of the two unique components ($U_X + U_Y$). A positive
 450 value indicates that the model overestimates a particular component at the expense of
 451 a different information type. The partitioning functional performance for a pair of sources
 452 is defined as the sum of the absolute values of the three pairwise measures as follows:

$$A_{f,Ipart_{i,j}} = |A_{f,S_{i,j}}| + |A_{f,R_{i,j}}| + |A_{f,U_{i,j}}| \quad (9)$$

453 This measure ranges from 0, for a model that exactly reproduces the observed information
 454 components, to 2, for a model that entirely substitutes one type of information for an-
 455 other or a combination of other information types. For instance, if the observed system
 456 shows that $U = 1$ (all information is unique), but a model system estimates $S = 1$ (that
 457 all information is synergistic), this leads to $A_{f,S} = 1$, $A_{f,U} = -1$ and $A_{f,Ipart} = 2$.
 458 While the individual source level identifies how the ranking of modeled variable impor-
 459 tance differs from observations, this pairwise level identifies how the model is interpret-
 460 ing information provided by combinations of sources.

461 At the highest “whole model” level of analysis, we calculate average overall func-
 462 tional performance across all individual ($A_{f,MI}$) and pairs of sources ($A_{f,Ipart}$) as fol-
 463 lows:

$$A_{f,MI,tot} = \frac{\sum_{i=1}^n (1 - |A_{f,MI_i}|)}{n}, \quad (10)$$

464 and

$$A_{f,Ipart,tot} = \frac{\sum_{i=1}^{n-1} \sum_{j=i+1}^n (2 - A_{f,Ipart_{i,j}})}{(n^2 - n)}, \quad (11)$$

465 where n is the number of source variables. $A_{f,MI,tot}$ ranges from $-\infty$ to 1 and $A_{f,Ipart,tot}$
 466 ranges from 0 to 2. We note that these measures are the originally defined individual and
 467 pairwise performance measures subtracted from 1 or 2, in order to align higher values
 468 with “best” model performance. In other words, a value of 1 (or 2 for $A_{f,Ipart,tot}$) now
 469 corresponds to a perfect match of modeled values to the observed data (Table 3). This
 470 level of functional performance metrics gauges the model’s overall ability to replicate the
 471 observed interactions. Figure 3 and Table 3 indicate the different levels of functional and
 472 predictive performance analysis.

Table 3: Summary of predictive and functional performance metrics.

Metric	Range	Best Performance	Eq. No.	Description
NSE	$-\infty$ to 1	1	1	Nash-Sutcliffe Efficiency (predictive)
KGE	$-\infty$ to 1	1	2	Kling-Gupta Efficiency (predictive)
A_H	$-\infty$ to 1	0	4	Normalized difference in entropy between observed and modeled (predictive)
$A_{f,MI}$	$-\infty$ to 1	0	6	MI difference for individual source (functional)
$A_{f,S_{i,j}}, A_{f,R_{i,j}}, A_{f,U_{i,j}}$	-1 to 1	0	8	Information partitioning components difference for a pair of sources (functional)
$A_{f,Ipart_{i,j}}$	0 to 2	0	9	Overall information component difference for a pair of sources (functional)
$A_{f,MI,tot}$	$-\infty$ to 1	1	10	Average functional performance of individual source level across all driving sources
$A_{f,Ipart,tot}$	0 to 2	2	11	Average functional performance across all pairs of sources for overall information partitioning

473 3 Results

474 3.1 Predictive Performance

475 NSE and KGE values are higher for local relative to regional training across all
 476 ML models and sites (Figure 4a). This implies that local training allows the models to

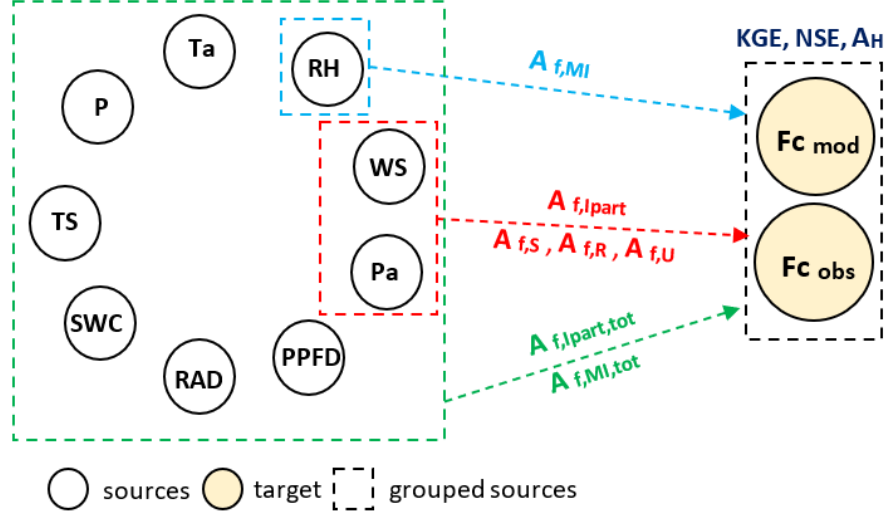


Figure 3: Illustration of functional and predictive performance. Nodes represent driving sources and target variables, and arrows represent different levels of functional performance. Predictive performance (NSE and KGE and A_H) measure agreement between observed and modeled values (Equations 1, 2, and 4). Blue, red, and green links show relationships that can be captured by functional performance metrics at different levels (Table 3).

477 better capture certain characteristics of each site. The regional model performance may
 478 stem from the limitations of this study, mainly a relatively small number of sites and site-
 479 years. A more extensive dataset encompassing multiple sites over varied temporal spans
 480 may provide the model with a broader range of conditions and variability, enabling it
 481 to generalize more effectively.

482 Meanwhile, we find that the A_H of local models is higher than that of regional mod-
 483 els (Figure 4b). A negative A_H occurs when $H_{mod} > H_{obs}$. This means that regional
 484 models actually introduce greater variability or uncertainty in Fc relative to observations.
 485 It is important to note that a negative A_H does not indicate “inferior” performance, since
 486 values close to zero represent “best” performance where the models reproduce the observed
 487 $H(Fc)$. While regional models over-estimate uncertainty in Fc , locally trained
 488 models underestimate uncertainty to a similar degree (Figure 4b).

489 When comparing performances of the three different models, RF (square markers
 490 in Figure 4a) consistently exhibits higher NSE and KGE values across all sites and both
 491 training experiences. This indicates the robustness of the RF model irrespective of the
 492 scale of the training data. Moreover, RF generally performs well in capturing the uncer-
 493 tainty in the observed Fc in both local and regional scales (square markers, Figure 4b).
 494 RF models have the best A_H performance for both regional and local models, indicat-
 495 ing their ability to replicate the observed entropy of Fc .

496 MLR (circle markers in Figure 4) performance varies highly between sites. For some
 497 sites, the NSE values are very low, especially for regional training, suggesting MLR does
 498 not capture the specific behaviors of those sites effectively. The negative NSE values in-
 499 dicate that a mean predictor would have been better for most sites. Meanwhile, KGE
 500 values fall closer to the 1:1 line of Figure 4a, indicating that the KGE metric does not
 501 distinguish as many differences between regional and local training. Similarly, A_H for

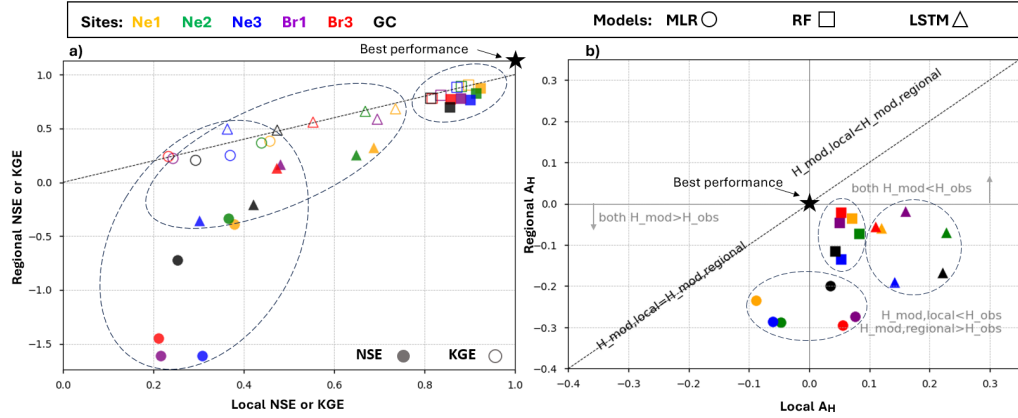


Figure 4: Predictive performance, (a) NSE (filled markers) and KGE (empty markers), and (b) the normalized difference in entropy between observed and modeled values (A_H) of three different models (MLR, RF, and LSTM, marker shapes) trained on local and regional data for six different sites (Table 1). Colors denote sites. The 1:1 line indicates equal performance for local and regional models.

502 the MLR model has the most spread between the study sites. For Nebraska sites (Ne1,
 503 Ne2, and Ne3), MLR has negative A_H values, which suggests that MLR model’s outputs
 504 for these sites are more uncertain compared to the observed data. On the other hand,
 505 MLR for the other sites show positive A_H values.

506 LSTM (triangle markers in Figure 4a) results in NSE and KGE values between those
 507 of RF and MLR. For some sites, performance is close to that of the RF. This suggests
 508 that LSTMs can model temporal patterns at individual sites to some extent, and is al-
 509 ways better than a mean predictor, but it never outperforms the RF model given the same
 510 training data. Given that LSTMs can model temporal sequences, the varied performance
 511 suggests that while some regional patterns are temporal, others might be non-sequential.
 512 We also find similar behaviour for LSTM as RF in capturing the entropy of observed Fc ,
 513 except for more variability between sites. When models are trained locally, LSTM mod-
 514 els tend to produce outputs that are less uncertain, or more predictable, than the observed
 515 data ($A_H > 0$). When models are trained regionally, LSTM outputs are more uncer-
 516 tain than observations. This difference between local and regional training for both LSTM
 517 and RF indicates that the regional training enables the model to produce more variable
 518 outputs, while local training leads to a more restricted range of Fc .

519 3.2 Functional Performance

520 At the individual and pairwise level, we focus on a single site, Ne1, as the site with
 521 the highest predictive performance and few gaps in forcing variables (WS and $NETRAD$).
 522 Other sites show similar patterns in mutual information and information decomposition
 523 measures, and we present full results for these in the Supplementary Information (SI Fig-
 524 ures S3-S18).

525 3.2.1 Individual Source Level

526 Each variable is ranked based on the average observed MI across all sites (Figure
 527 5a, black line). TS and Ta share the most information with Fc , indicating a strong de-
 528 pendence on fluctuations in both air and soil temperatures. The next variables that share
 529 information with Fc are radiation variables, $NETRAD$ and $PPFD$. Meanwhile, precip-

530 itation (P) is a very weak predictor of Fc , which is expected since sub-daily precipita-
 531 tion contains many zero-values, leading to low entropy. Instead, we see that SWC shares
 532 more information with Fc , indicating that moisture available to roots and soil is impor-
 533 tant. Meteorological variables Pa , RH , and WS are relatively weak individual predictors.
 534 Models either overestimate or underestimate these mutual information values, resulting
 535 in a different ranking of variables for each model type (Figure 5a).

536 We use $A_{f,MI}$ to assess the extent to which mutual information matches with the
 537 observed target variable at Ne1 site (Figure 5b) and at other sites (SI Figure S3-S6). Higher
 538 absolute $A_{f,MI}$ values suggest that the modeled value is far from the observed value. If
 539 $A_{f,MI}$ is negative, the model overestimates the mutual information of observed Fc (an
 540 overly deterministic model), and if $A_{f,MI}$ is positive, the model underestimates observed
 541 mutual information (an overly random model).

542 The MLR model tends to underestimate mutual information (positive $A_{f,MI}$) for
 543 TS , Ta , SWC , Pa , WS , and P while overestimating for $NETRAD$, and $PPFD$, particu-
 544 larly for local training (Figure 5b, blue circles). MLR also shows the largest spread in
 545 over and underestimates of mutual information. The LSTM model for local training has
 546 a negative $A_{f,MI}$ for the most relevant drivers, but this is improved under regional train-
 547 ing (Figure 5b, green triangles). The RF models closely replicate observed mutual information
 548 for both regional and local training (Figure 5b, red and orange squares). This highlights
 549 the power of RF in capturing the intricacies and dependencies within Fc regardless of
 550 the scale of the training data. Here we discuss the model representation of individual forc-
 551 ing variables.

- 552 • TS , Ta : While local and regional MLR model greatly underestimates the influence
 553 of temperature variables, the locally trained LSTM model overestimates it to a
 554 similar degree. In other words, the local LSTM model correctly identifies these
 555 as top sources of information to Fc , but to a more extreme degree, while the MLR
 556 models do not consider temperature as a top source.
- 557 • $NETRAD$ and $PPFD$: For local MLR, $A_{f,MI}$ is large and negative, indicating that
 558 the model overestimates the influence of radiation variables, and interprets them
 559 as the most important forcing variables instead of temperatures. However for the
 560 regional MLR, $A_{f,MI}$ is close to zero, indicating that the regional model mitigates
 561 this over-estimation. The only model that slightly underestimates mutual information
 562 from these variables is the regionally trained LSTM.
- 563 • SWC and P : Precipitation is a very weak driver according to both observations
 564 and models (Figure 5a), but models nearly always underestimate mutual information.
 565 They also underestimate information from SWC , except for the regionally trained
 566 LSTM. This indicates that models may lack sensitivity to moisture variability.
- 567 • WS : Across all models, the $A_{f,MI}$ values are fairly consistent, small, and positive,
 568 indicating all models slightly underestimate the influence of wind speed.
- 569 • Pa and RH : The locally trained MLR model shows the worst performance in terms
 570 of both over and under-estimating information from these variables.

571 These patterns are similar for other sites and under regional training (SI Figures
 572 S3-S6). This consistency suggests that the observed MI behaviors are not merely site-
 573 specific but possibly representative of broader environmental interactions. The key take-
 574 away is that all models overestimate the influence of certain drivers at the expense of
 575 others, but to different degrees. This understanding can be useful to refine models or test
 576 the sensitivity of certain drivers. However, this level of analysis may omit drivers that
 577 provide information jointly rather than individually.

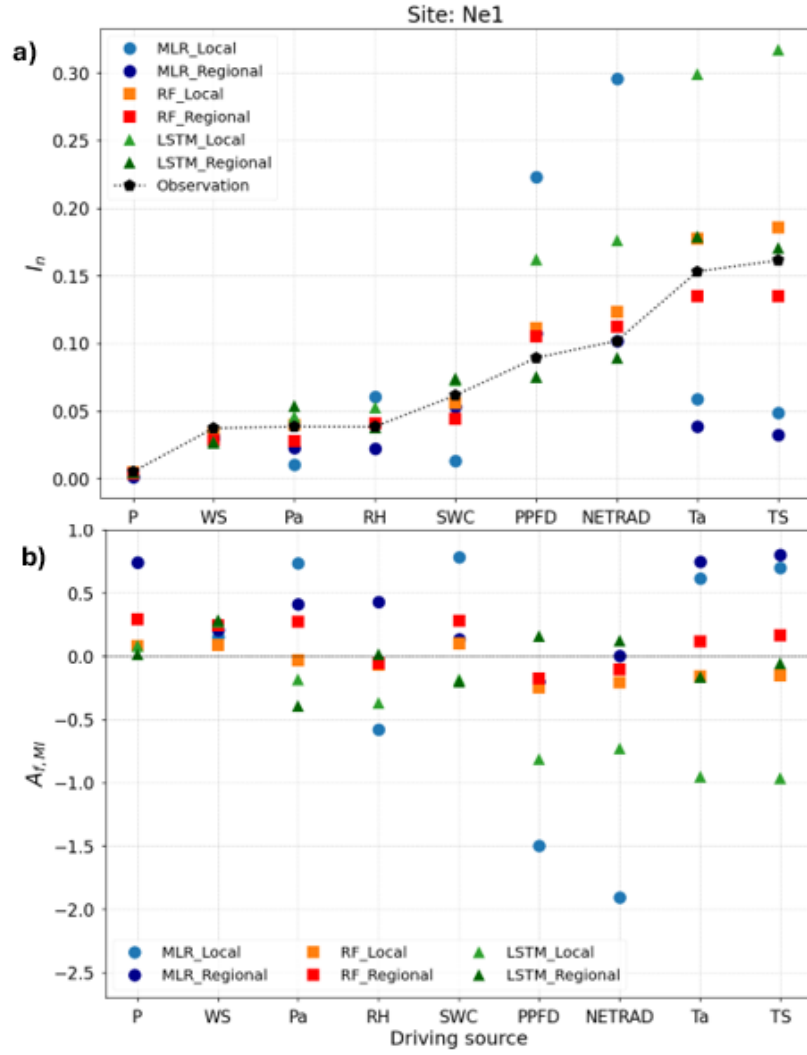


Figure 5: (a) Normalized mutual information (I_n) and (b) functional performance for individual variables ($A_{f,MI}$), Equation 6, for Multiple Linear Regression (MLR), Random Forest (RF), and Long Short-Term Memory (LSTM) models, under local and regional training at Ne1 site. Each variable is ranked (order on x-axis) based on the average observed MI across all sites (black line).

578

3.2.2 Pairwise and Model Level

579

580

581

582

583

584

585

586

587

588

589

In the observed data, most variable pairs provide synergistic (S) or unique information (U) to Fc (Figure 6a-c). The only pairs that provide a large fraction of redundant information (R) are closely related pairs (Ta , TS) and ($PPFD$, $NETRAD$). However, we note that their redundancy is still less than 0.5 as a fraction of total information, and the other half of the information they provide is U . Precipitation (P) provides the most U when paired with other variables (Figure 6c), but as found in the previous analysis of individual sources, the actual amount of information it provides is very small due to its low entropy. Meanwhile, Ta tends to provide the next highest fraction of U when paired with other sources, while RH and WS to provide S along with other sources. In general, regardless of the amount of information that sources provide, here we find that they mainly provide unique and synergistic information types.

590

591

592

593

594

595

596

597

598

All models tend to underestimate S (negative $A_{f,S}$, Figure 6d,g,j) for most variable pairs, at the expense of overestimating U (positive $A_{f,U}$, Figure 6f,i,l). For example, in the MLR model, RH greatly underestimates S and overestimates U when paired with other variables (Figure 6d,f). While the underestimation of synergistic relationships is widespread, the overestimation of redundancy only tends to occur for the most correlated variable pairs, specifically (Ta , TS) and ($PPFD$, $NETRAD$). This indicates that models rely excessively on these correlations, which results in an overemphasis in R . In other words, the observed relationship between these variables is not as redundantly informative for Fc as the model predicts, but they are instead more unique predictors.

599

600

601

602

603

604

605

606

607

608

609

Essentially, depending on the variable pair, the model either uses information uniquely where observations show a synergistic type of relationship, or uses information redundantly where observations show both unique and redundant contributions. The MLR model shows the largest trade-off between S and U partitioning performances (Figure 6d,f), followed by LSTM. Meanwhile, MLR is the only model that does not overestimate R provided by (Ta , TS), and in fact captures all information types accurately for this pair. However, we note that this MLR model also greatly underestimates the individual information components shared by each of these variables to the target (Figure 5). In other words, the MLR model greatly underestimates the importance of these temperature variables as predictors of Fc , but does reflect the mechanism by which they jointly provide information.

610

611

612

613

614

615

616

While broad patterns in information decomposition components are similar between models, there are several differences. For example, consider the (SWC , Ta) pair (bottom corner in all Figure 6 panels). For MLR, the information components are reproduced fairly accurately. For RF, U is overestimated at the expense of S to a minor degree. For LSTM, this occurs to a higher degree and R is also slightly overestimated. Meanwhile the MLR model greatly overestimates U from the pair (RH , $NETRAD$) at the expense of S , while the other two models have a similar but less extreme pattern.

617

618

619

620

621

622

623

624

625

626

627

When we consider the combined partitioning performance, $A_{f,Ipart}$ for each variable pair, the RF model has the best model performance, as it shows more $A_{f,Ipart}$ values close to zero (Figure 7). The MLR shows the most variability between pairs of sources, such that some pairs have very good functional partitioning performance and others have values of $A_{f,Ipart}$ greater than 1, indicating that over half of the information decomposition is misrepresented by the model. RH , $NETRAD$, and $PPFD$ have particularly poor functional performance when combined with other sources for the MLR model. The LSTM model also has lower functional partitioning performance relative to RF, but behavior is more even between pairs of variables. Precipitation (P) always has the best functional performance when paired with other variables, but it is the weakest source and provides very little information regarding Fc for either models or observations.

When we consider other sites (SI Figures S7-S12), we find similar patterns in pairwise functional performance, specifically the overestimation of U at the expense of S and overestimation of R for correlated source pairs. However, we find that regionally trained models diminish some of the issues observed in the localized models. The broader dataset that regional training offers seems to provide a more balanced representation, allowing models to discern patterns beyond local-specific interactions. The regional model also corrects the balance between synergy and unique contributions, leading to a more accurate representation of how these variables interact. This trend is especially evident in the LSTM model, which demonstrates enhanced functional performance under regional training (SI Figures S13-S18). In terms of site differences, we find that regional LSTM model has the best model performance at Ne1 and Ne3 sites and RF model has the best performance among other sites.

When we calculate average overall functional performance at individual level ($A_{f,MI,tot}$), we find patterns that are similar to the average pairwise functional performance ($A_{f,Ipart,tot}$) (Figure 8). Specifically, local RF models perform slightly better than regional RF models on the individual level, while regional MLR and LSTM models generally perform better than the local models (Figure 8a). However, at the pairwise level, regional models consistently outperform their local equivalents (Figure 8b). This contrasts with trends observed in the predictive performance metrics (Figure 4), where local training led to higher NSE values relative to regional training.

Among all models, the RF model demonstrates the best performance, both at individual and pairwise levels (square markers in Figure 8). For individual sources, local RF models have better performance than the regional models. But when considering pairwise relationships, the regional RF model shows superior performance. On the other hand, the MLR model exhibits the lowest performance values at the individual level but performs more similarly to LSTM when considering pairwise relationships. The regional LSTM model also shows good performance at both the individual and pairwise levels. However, the performance of the local LSTM model varies more across different sites at the individual level, while the pairwise performance is more consistent for the regional model. This analysis highlights that changes in one aspect of functional performance do not necessarily translate to similar changes in other aspects.

3.3 Relationship between Predictive and Functional Performance

The relationship between predictive performance and functional performance provides insights into how a model balances replicating the observed data and its ability to capture observed relationships. As an illustration, we first focus on two key metrics: the KGE , representing predictive performance, and the $A_{f,Ipart,tot}$, indicating functional performance (Figure 9). For the 6 sites, two training types, and 3 model types, we have 36 total model runs for this comparison. All models show higher functional performance under regional training, but differences in KGE are on a site-by-site basis. The Ne1 site tends to be the highest performing site for all models in terms of KGE , but varies between models for $A_{f,Ipart,tot}$.

The functional and predictive performances for RF are both high relative to other models, and there is little variability between sites. However, there is an apparent trade-off between functional and predictive performance, in that sites with the highest KGE tend to have lower $A_{f,Ipart,tot}$. Meanwhile, there is a slight positive trend for locally trained LSTM and MLR models, where higher functional and predictive performances go together (Figure 9).

A correlation analysis shows that while functional and predictive performance measures tend to be correlated to each other (Figure 10a,c), there are fewer statistically significant ($p < 0.05$) correlations between the two types (Figure 10b). This correlation analysis is based on all 36 model cases (3 ML models, regional and local, and 6 sites) so

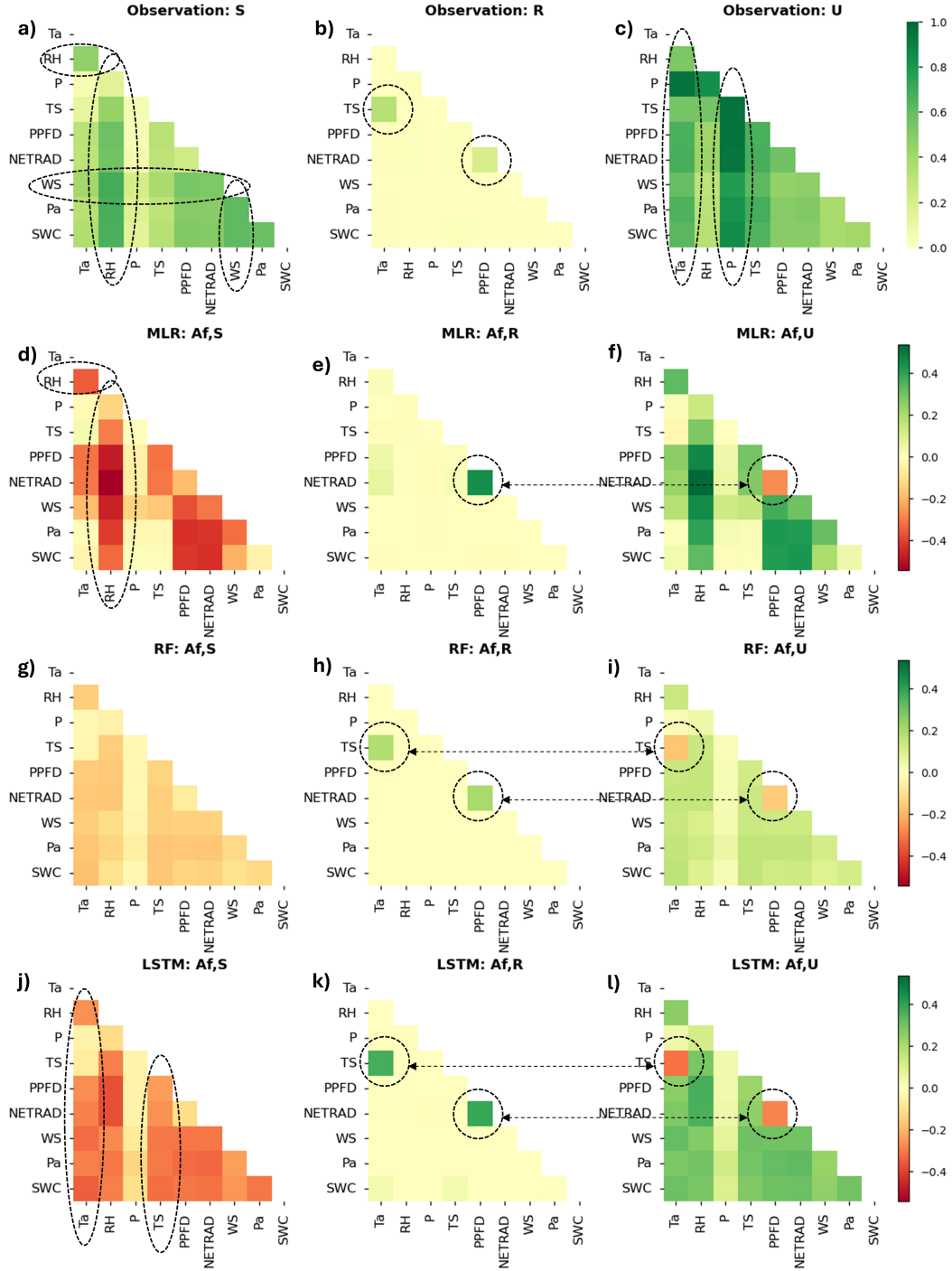


Figure 6: Observed pairwise (a) synergistic ($S_{i,j}$), (b) redundancy ($R_{i,j}$), and (c) uniqueness ($U_{i,j}$) information flow at Ne1 site. Pairwise functional performance of three models under local training experience at Ne1 site. The heat-map represents the relative difference in information decomposition partitioning measures ($A_{f,S_{i,j}}$, $A_{f,R_{i,j}}$, and $A_{f,U_{i,j}}$) between modeled and observed data for each pair of forcing variables. Positive values (green) in (d)-(l) indicate that the model overestimates the information type, while negative values (red) indicate underestimations.

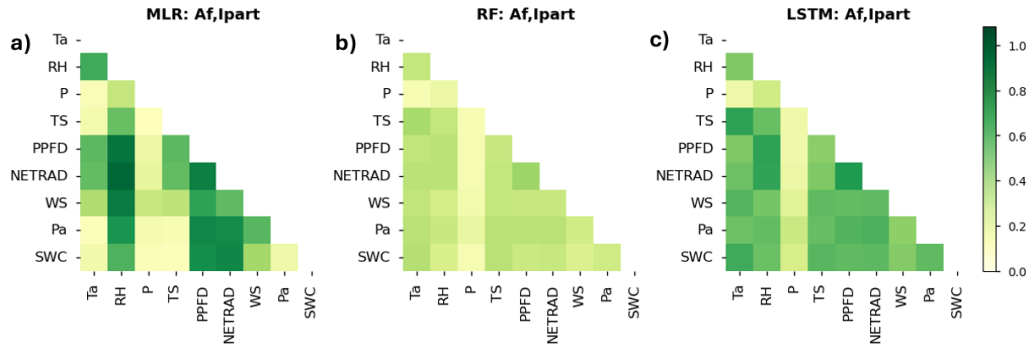


Figure 7: Pairwise functional partitioning performance $A_{f,Ipart_{i,j}}$ for (a) MLR, (b) RF, and (c) LSTM models under local training experience at Ne1 site. Values close to zero indicate optimal partitioning performance for a given pair.

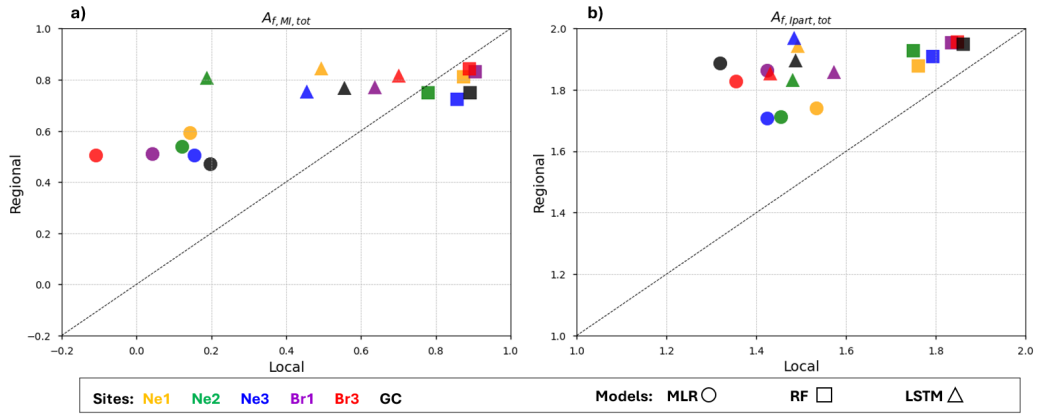


Figure 8: The whole model functional performance for (a) across all individual sources, $A_{f,MI,tot}$ and (b) across all pairs of sources, $A_{f,Ipart,tot}$, of three model types under two training experiences, local and regional, for six sites.

679 does not distinguish trends for a single model type or training experience. As illustrated
 680 in Figure 9, there may be a stronger correlation within a given model type and training.
 681 We split the KGE into its three constituent components, where high values of each term
 682 indicate “best” model performance. Similarly, the A_H measure of entropy and functional
 683 performance metrics are scaled so that high values indicate best performance, and pos-
 684 itive correlations are easy to interpret.

685 Predictive performance metrics are positively correlated, except for the α , or vari-
 686 ability, term of KGE with NSE and A_H . We find that the correlation component (r) is
 687 most correlated to the total KGE. Meanwhile, β and α terms are less correlated to KGE,
 688 and individual KGE components are less correlated to each other. This indicates that
 689 the correlation between observed and modeled Fc is the most predictive of KGE for these
 690 models. Meanwhile, both β and r terms are highly correlated with NSE. This highlights
 691 that the NSE is sensitive to the bias between model and observations and their corre-
 692 lation. The two full model functional performance metrics are also positively correlated
 693 (Figure 10c), indicating that models with high performance in terms of individual sources
 694 also reproduce pairwise relationships well.

695 In terms of correlations between functional and predictive measures (Figure 10b),
 696 5 of the 12 possible correlations are positive and the other 7 are non-statistically signif-
 697 icant, indicating that higher predictive performance is generally but not always associ-
 698 ated with higher functional performance. The KGE α , or variability, component shows
 699 the highest correlation with functional measures, followed by the total KGE. This leads
 700 us to interpret that α is the most indicative of functional performance, and is the basis
 701 for the correlation between KGE and the functional measures. This indicates that mod-
 702 els that reproduce the standard deviation of observed Fc , upon which α is based, also
 703 tend to reproduce observed forcing- Fc relationships at both a pairwise and individual
 704 level. Meanwhile, A_H , which is based on the difference in entropies of observed and mod-
 705 eled Fc , does not have a statistically significant correlation with functional performance.
 706 This illustrates that a model can reproduce the entropy of the observation, but not re-
 707 produce the distribution or functional relationships. In other words, the entropy is a sum-
 708 mary statistic that does not necessarily indicate whether the model correctly replicates
 709 other features of the distribution of the data. No functional performance measures are
 710 correlated to the NSE, the β , or bias component of KGE, or A_H . This could be related
 711 to the linearity of these predictive performance measures that may not reflect nonlinear
 712 and joint interactions detected with mutual information. Additionally, we note that IT-
 713 based measures consider the distribution of the data but not the actual values, such that
 714 an IT measure would not capture a constant bias between two variables.

715 4 Discussion

716 Many machine learning approaches have been applied across major sub-domains
 717 of Earth system science and are increasingly being integrated into operational schemes
 718 and used to discover patterns, improve our understanding, and benchmark physically-
 719 based models. Ideally, ML models generate predictive models devoid of any presumptions
 720 on the underlying ecological structure or the mathematical representation of processes
 721 and interactions in an ecosystem. However, this lack of presumptions is correlated to a
 722 lack of understanding of whether and how these models are capturing functional relation-
 723 ships that exist in nature. The results of this study emphasize that functional performance—how
 724 accurately models capture the underlying relationships between variables—can be paired
 725 with more traditional metrics of model performance. By evaluating both functional and
 726 predictive aspects and their interrelationship, we can obtain a wider perspective on the
 727 strengths and limitations of different machine learning models. This multi-tiered approach
 728 not only can be used to explore the behavioral ranges for both machine learning and process-
 729 based models but also guides model development by highlighting model deficiencies based
 730 on information flow pathways that would not be apparent based on existing measures.

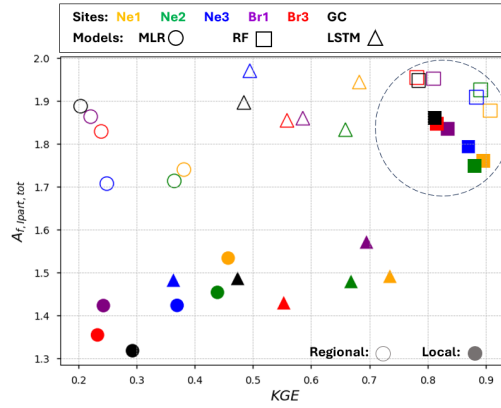


Figure 9: Predictive performance (KGE) and the overall model level of functional performance ($A_{f,Ipart,tot}$) of three model types under two training experiences, local (filled markers) and regional (empty markers).

731 Since ML-predicted fluxes can be used as benchmarks for physical land-surface and cli-
 732 mate model evaluation (Q. Zhou et al., 2019; Anav et al., 2015; Best et al., 2015), it is
 733 valuable to understand nuances in their behavior.

734 While earlier studies on the CO_2 balance of vegetated surfaces applied linear re-
 735 gression for estimating the carbon fluxes (Jensen et al., 1996; Xu & Qi, 2001; Burrows
 736 et al., 2005), artificial neural network (ANN) and the support vector machine (SVM) meth-
 737 ods have also been used to estimate terrestrial carbon fluxes and interpret the nonlin-
 738 ear relationship between ecosystem-based carbon fluxes and environment variables based
 739 on eddy covariance measurements (Papale & Valentini, 2003; Dou & Yang, 2018). For
 740 example, an ANN was able to filter out noise, predict the seasonal and diurnal variation
 741 of carbon fluxes, and extract patterns such as increased respiration in spring during root
 742 growth, which was formerly not well represented in carbon cycle models (Papale & Valen-
 743 tini, 2003). In this study, the Random Forest model showed both the highest functional
 744 and predictive performances, confirming that its better predictions really are associated
 745 with better process representations. The RF’s non-parametric nature means it makes
 746 fewer assumptions about the underlying relationships between variables, thus enabling
 747 it to proficiently model intricate, non-linear interactions. Meanwhile, linear regression
 748 had a wide spread in performance levels between individual sites, and greatly overesti-
 749 mated the influence of radiation drivers that are highly linearly correlated to carbon flux.
 750 The LSTM model performance varied greatly between local and regional training, indi-
 751 cating that its functional performance benefited from training data from multiple sites.

752 Complex and nonlinear drivers such as meteorology, soils, vegetation, and available
 753 energy cause Fc to be highly variable in space and time and challenging to measure and
 754 model (Huang et al., 2017; He et al., 2018; Chen et al., 2020; Dou & Yang, 2018). Sev-
 755 eral approaches have been developed to understand current and future terrestrial car-
 756 bon flux over the past several decades involving field observations (Falge et al., 2002; Xiao
 757 et al., 2011), large-scale remote sensing (Xiao et al., 2019), process-based modeling (D. Wang
 758 et al., 2011; Dunkl et al., 2021), or a combination of these methods (Vetter et al., 2008;
 759 Jung et al., 2011). Our study sheds further light on how forcing variables provide information
 760 to observed carbon fluxes. We found that temperature and radiation variables are most
 761 highly informative of Fc , followed by moisture-related variables such as RH and SWC .
 762 While many variables have a diurnal pattern, including Fc , we find that forcing variables
 763 tend to provide synergistic or unique information, rather than redundant information,

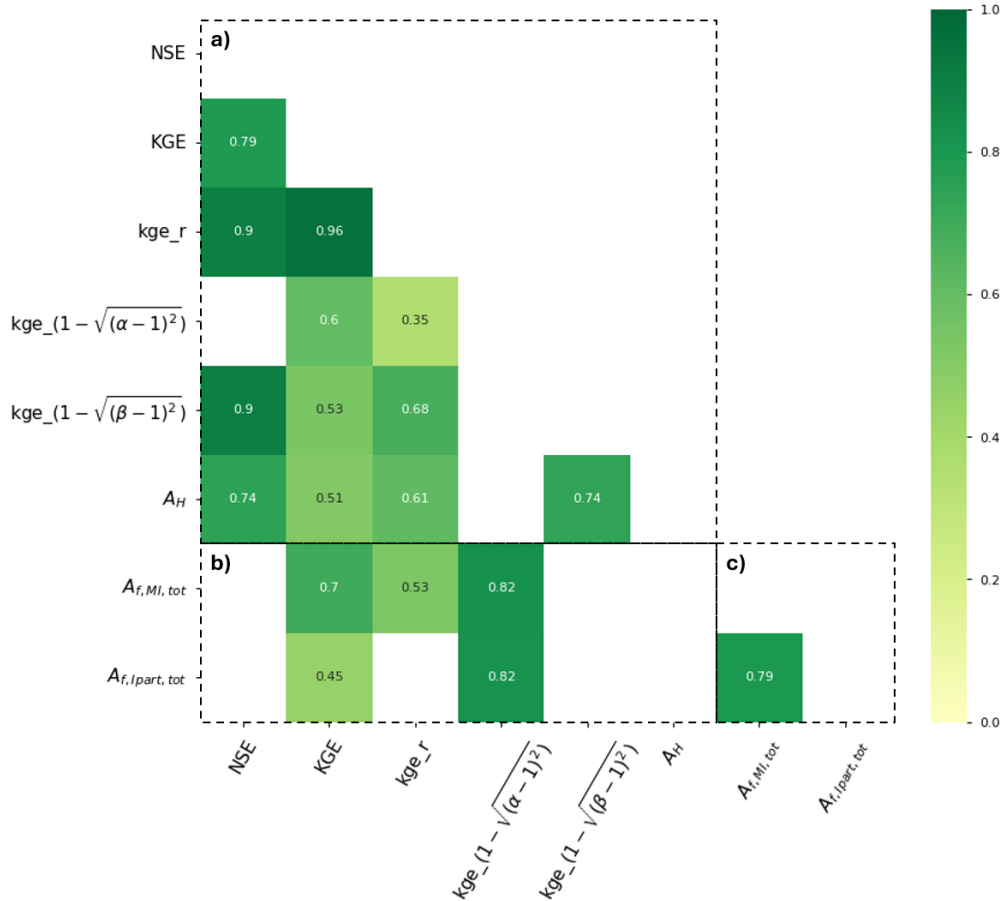


Figure 10: Correlation (p -value < 0.05) between performance metrics listed in Table 3 (scaled so that larger values always correspond to best performance), for the 36 model runs performed in this study. (a) and (c) separate correlations within predictive and functional categories, respectively, while (b) shows correlations between functional and predictive metrics.

764 indicating that the overlap in information content is relatively low. Meanwhile, RH
 765 is relatively weak as an individual source, but we found that it provides synergistic information
 766 when paired with many other sources. This indicates that the relevance of a variable like
 767 RH could be underestimated in an analysis that did not consider multivariate interac-
 768 tions, since it is a weak individual source but enhances the information content of other
 769 sources. In terms of modeling, we found that MLR, the simplest model, overestimates
 770 information from radiation variables and underestimates information from temperatures.
 771 This suggests that MLR captures the strongly linear diurnal pattern between energy avail-
 772 ability and carbon flux, but misses a stronger but more nonlinear relationship with tem-
 773 perature due to the limitations in its parameterization. Finally, the tendency of all mod-
 774 els to underestimate information from SWC indicates that water availability to plants
 775 is a complex driver of Fc that is difficult to capture in a functional form.

776 We note several limitations and assumptions that could be improved in future work.
 777 Future research could delve deeper into variations between sites, exploring what site-specific
 778 features influence model performance. One of the uncertainties of using flux tower mea-
 779 surements to estimate Fc is the impact of shifting land cover on the accuracy of the ob-

780 observations. The land-atmosphere exchange fluxes that generate carbon flux are influenced
781 by the dynamic upwind surface area, called the flux footprint, which can exhibit spatial
782 heterogeneities (Hernandez Rodriguez et al., 2023; Leclerc & Foken, 2014). As a result,
783 fluxes from different sources can mix at the observation point, introducing uncertainty
784 into the measurements. Meanwhile, this study assumes that the mix of crop types be-
785 tween sites and between observation time points leads to similar causal interactions be-
786 tween forcing variables and carbon flux. We also did not specifically focus on the opti-
787 mization of hyperparameters within each ML model, which could have an effect on func-
788 tional and predictive performance. Moreover, the precision and general quality of the
789 forcing variables and F_c are important as they have underlying uncertainties and have
790 been gap-filled, and our interpolation methods may have more effect on some model struc-
791 tures than others and future research could explore how models use information encoded
792 in forcing data (Farahani et al., 2022). We also note that the MLR performance can be
793 significantly influenced by multicollinearity among the forcing variables, and we did not
794 test for this aspect. In terms of data size, we only considered six locations and approx-
795 imately 50-site years, so further studies could more specifically consider the effect of in-
796 creasingly large and diverse training datasets on model functional behaviors. Finally, the
797 models evaluated represent just a fraction of the available algorithms, and we do not con-
798 sider a wider range of ML and process-based models.

799 While predictive and functional metrics tend to be positively correlated, there are
800 cases where a model change could be made that appears to improve predictions, but sac-
801 rifices a functional relationship. For example, the finding that regionally trained mod-
802 els tend to have improved functional performance indicates that these models can dis-
803 cern patterns beyond local-specific interactions. However, in this study the predictive
804 performance of regional models was somewhat lower relative to single-site models, po-
805 tentially marking a trade-off between functional and predictive performance. A “perfect”
806 model should replicate all functional relationships as they are observed, but it still may
807 not have perfect predictive performance due to missing information. In other words, the
808 forcing variables simply do not contain all the information necessary to make a perfect
809 accurate prediction. In this way, information-based metrics of functional performance
810 provide a type of upper bound for predictive performance. This underscores the need
811 for a nuanced approach to model selection. For an ungauged site with no validation data,
812 a regionally trained model is likely the most applicable since it has a stronger functional
813 performance and can reproduce processes as they are observed. The LSTM model was
814 the most responsive to changes in training data size, which could relate to its complex-
815 ity and need for many datasets to learn time-dependent interactions.

816 5 Conclusion

817 Predictive accuracy is just one facet of modeling complex ecohydrologic systems.
818 Meanwhile, functional performance metrics capture how a model grasps the intricate re-
819 lationships among variables. In order to use models for prediction in unseen conditions,
820 and compare between machine learning and physically based model structures, we need
821 to ensure that models don’t just predict well, but also understand and represent the un-
822 derlying processes effectively. In other words, understanding the why and how behind
823 predictions can be as vital as the predictions themselves. In this study, the Random For-
824 est model emerged as a consistently reliable model in terms of both predicting carbon
825 fluxes and reproducing observed functional relationships at multiple levels. Meanwhile,
826 a simple linear regression will overestimate the influence of variables with the most lin-
827 ear relationships to the target outcome. All models in this study had the common fea-
828 ture of underestimating synergistic interactions and overestimating unique ones. This
829 indicates that all models are not quite capturing information flows at higher levels, where
830 multiple sources provide information to the target jointly, and indicates that even the
831 models with the highest predictive performance could be improved. Similarly, while per-

832 performance measures tend to be correlated, no single performance measure captures the
 833 effect of all the others. This study advocates for a combined approach to model evalu-
 834 ation and validation, which considers both predictive performance and how the model
 835 captures interactions in the ecohydrologic system.

836 Acknowledgments

837 M.A. Farahani and A.E. Goodwell acknowledge funding from NSF Grant EAR #2012850
 838 for the Critical Interface Network for Intensively Managed Landscapes (*CINet*) and the
 839 NASA New Investigator Grant #80NSSC21K0934. Python codes for analyses presented
 840 here are available on at https://github.com/allisongoodwell/Farahani_CarbonML2023.

841 References

- 842 Anav, A., Friedlingstein, P., Beer, C., Ciais, P., Harper, A., Jones, C., . . . Zhao, M.
 843 (2015). Spatiotemporal patterns of terrestrial gross primary production: A
 844 review. *Reviews of Geophysics*, *53*(3), 785-818. doi: [https://doi.org/10.1002/](https://doi.org/10.1002/2015RG000483)
 845 [2015RG000483](https://doi.org/10.1002/2015RG000483)
- 846 Balasis, G., Donner, R. V., Potirakis, S. M., Runge, J., Papadimitriou, C., Daglis,
 847 I. A., . . . Kurths, J. (2013). *Statistical mechanics and information-theoretic*
 848 *perspectives on complexity in the Earth system* (Vol. 15) (No. 11). doi:
 849 [10.3390/e15114844](https://doi.org/10.3390/e15114844)
- 850 Bassiouni, M., & Vico, G. (2021). Parsimony versus predictive and functional perfor-
 851 mance of three stomatal optimization principles in a big-leaf framework. *New*
 852 *Phytologist*, 0–2. doi: [10.1111/nph.17392](https://doi.org/10.1111/nph.17392)
- 853 Bennett, A., Nijssen, B., Ou, G., Clark, M., & Nearing, G. (2019). Quantifying pro-
 854 cess connectivity with transfer entropy in hydrologic models. *Water Resources*
 855 *Research*, *55*(6), 4613-4629. doi: [10.1029/2018WR024555](https://doi.org/10.1029/2018WR024555)
- 856 Best, M. J., Abramowitz, G., Johnson, H. R., Pitman, A. J., Balsamo, G., Boone,
 857 A., . . . Vuichard, N. (2015). The plumbing of land surface models: Benchmark-
 858 ing model performance. *Journal of Hydrometeorology*, *16*(3), 1425 - 1442. doi:
 859 <https://doi.org/10.1175/JHM-D-14-0158.1>
- 860 Bollt, E. M., Sun, J., & Runge, J. (2018). Introduction to focus issue: Causation
 861 inference and information flow in dynamical systems: Theory and applications.
 862 *Chaos: An Interdisciplinary Journal of Nonlinear Science*, *28*(7), 075201. doi:
 863 [10.1063/1.5046848](https://doi.org/10.1063/1.5046848)
- 864 Breiman, L. (2001). Random forests. *Machine Learning*, *45*(1), 5-32. doi: [10.1023/A:](https://doi.org/10.1023/A:1010933404324)
 865 [1010933404324](https://doi.org/10.1023/A:1010933404324)
- 866 Burrows, E. H., Bubier, J. L., Mosedale, A., Cobb, G. W., & Crill, P. M. (2005). Net
 867 ecosystem exchange of carbon dioxide in a temperate poor fen: a comparison
 868 of automated and manual chamber techniques. *Biogeochemistry*, *76*(1), 21–45.
- 869 Chen, N., Wang, A., An, J., Zhang, Y., Ji, R., Jia, Q., . . . Guan, D. (2020). Modeling
 870 canopy carbon and water fluxes using a multilayered model over a temperate
 871 meadow in inner mongolia. *International Journal of Plant Production*, *14*(1),
 872 141-154. doi: [10.1007/s42106-019-00074-4](https://doi.org/10.1007/s42106-019-00074-4)
- 873 Cover, T. M., & Thomas, J. A. (2012). *Elements of information theory*. John Wiley
 874 & Sons.
- 875 Dou, X., & Yang, Y. (2018). Comprehensive evaluation of machine learning
 876 techniques for estimating the responses of carbon fluxes to climatic forces in
 877 different terrestrial ecosystems. *Atmosphere*, *9*(3). doi: [10.3390/atmos9030083](https://doi.org/10.3390/atmos9030083)
- 878 Dou, X., Yang, Y., & Luo, J. (2018). Estimating forest carbon fluxes using ma-
 879 chine learning techniques based on eddy covariance measurements. *Sustainabil-*
 880 *ity*, *10*(1). doi: [10.3390/su10010203](https://doi.org/10.3390/su10010203)
- 881 Drewry, D. T., Kumar, P., Long, S., Bernacchi, C., Liang, X. Z., & Sivapalan, M.
 882 (2010a). Ecohydrological responses of dense canopies to environmental variabil-

- ity: 1. Interplay between vertical structure and photosynthetic pathway. *Journal of Geophysical Research: Biogeosciences*, 115(4). doi: 10.1029/2010JG001340
- 883
884
885 Drewry, D. T., Kumar, P., Long, S., Bernacchi, C., Liang, X. Z., & Sivapalan, M.
886 (2010b). Ecohydrological responses of dense canopies to environmental vari-
887 ability: 2. Role of acclimation under elevated CO_2 . *Journal of Geophysical*
888 *Research: Biogeosciences*, 115(4), 1–22. doi: 10.1029/2010JG001341
- 889 Dunkl, I., Spring, A., Friedlingstein, P., & Brovkin, V. (2021). Process-based analysis
890 of terrestrial carbon flux predictability. *Earth System Dynamics*, 12(4), 1413–
891 1426. doi: 10.5194/esd-12-1413-2021
- 892 Dutta, D., Wang, K., Lee, E., Goodwell, A., Woo, D., Wagner, D., & Kumar, P.
893 (2017). Characterizing vegetation canopy structure using airborne remote
894 sensing data. *IEEE Transactions on Geoscience and Remote Sensing*, 55(2),
895 1160–1178. doi: 10.1109/TGRS.2016.2620478
- 896 Falge, E., Baldocchi, D., Tenhunen, J., Aubinet, M., Bakwin, P., Berbigier, P.,
897 ... Wofsy, S. (2002). Seasonality of ecosystem respiration and gross
898 primary production as derived from fluxnet measurements. *Agricultural*
899 *and Forest Meteorology*, 113(1), 53–74. (FLUXNET 2000 Synthesis) doi:
900 [https://doi.org/10.1016/S0168-1923\(02\)00102-8](https://doi.org/10.1016/S0168-1923(02)00102-8)
- 901 Farahani, M. A., Vahid, A., & Goodwell, A. (2022). Evaluating ecohydrological model
902 sensitivity to input variability with an information-theory-based approach. *En-*
903 *tropy*, 24(7). doi: 10.3390/e24070994
- 904 Franzen, S. E., Farahani, M. A., & Goodwell, A. (2020). Information flows: Char-
905 acterizing precipitation-streamflow dependencies in the Colorado headwaters
906 with an information theory approach. *Water Resources Research*, 56(10),
907 e2019WR026133. doi: <https://doi.org/10.1029/2019WR026133>
- 908 Goodfellow, I., Bengio, Y., & Courville, A. (2016). *Deep learning*. MIT Press.
909 (<http://www.deeplearningbook.org>)
- 910 Goodwell, A., & Bassiouni, M. (2022). Source relationships and model structures de-
911 termine information flow paths in ecohydrologic models. *Water Resources Re-*
912 *search*, 58(9). doi: <https://doi.org/10.1029/2021WR031164>
- 913 Goodwell, A., Jiang, P., Ruddell, B. L., & Kumar, P. (2020). Debates—does
914 information theory provide a new paradigm for Earth science? Causal-
915 ity, interaction, and feedback. *Water Resources Research*, 56(2). doi:
916 <https://doi.org/10.1029/2019WR024940>
- 917 Goodwell, A., & Kumar, P. (2017). Temporal information partitioning: Characterizing
918 synergy, uniqueness, and redundancy in interacting environmental variables. *Wa-*
919 *ter Resources Research*, 53(10), 5920–5942. doi: 10.1002/2016WR020218
- 920 Gupta, H. V., Kling, H., Yilmaz, K. K., & Martinez, G. F. (2009). Decomposi-
921 tion of the mean squared error and nse performance criteria: Implications for
922 improving hydrological modelling. *Journal of Hydrology*, 377(1), 80–91. doi:
923 <https://doi.org/10.1016/j.jhydrol.2009.08.003>
- 924 Hawkins, L. R., Bassouni, M., Anderegg, W. R. L., Venturas, M. D., Good, S. P.,
925 Kwon, H. J., ... Still, C. J. (2022). Comparing model representations of
926 physiological limits on transpiration at a semi-arid ponderosa pine site. *Jour-*
927 *nal of Advances in Modeling Earth Systems*, 14(11), e2021MS002927. doi:
928 <https://doi.org/10.1029/2021MS002927>
- 929 He, L., Li, J., Harahap, M., & Yu, Q. (2018). Scale-specific controller of carbon
930 and water exchanges over wheat field identified by ensemble empirical mode
931 decomposition. *International Journal of Plant Production*, 12(1), 43–52. doi:
932 10.1007/s42106-017-0005-8
- 933 Hernandez Rodriguez, L., Goodwell, A., & Kumar, P. (2023). Inside the flux footprint:
934 The role of organized land cover heterogeneity on the dynamics of observed
935 land-atmosphere exchange fluxes. *Agricultural and Forest Meteorology*. doi:
936 <http://dx.doi.org/10.2139/ssrn.4034618>
- 937 Hestness, J., Narang, S., Ardalani, N., Damos, G., Jun, H., Kianinejad, H., ...

- 938 Zhou, Y. (2017). *Deep learning scaling is predictable, empirically.*
- 939 Hochreiter, S., & Schmidhuber, J. (1997a). Long Short-Term Memory. *Neural Compu-*
940 *tation*, 9(8), 1735-1780. doi: 10.1162/neco.1997.9.8.1735
- 941 Hochreiter, S., & Schmidhuber, J. (1997b). Long Short-Term Memory. *Neural Compu-*
942 *tation*, 9(8), 1735-1780. doi: 10.1162/neco.1997.9.8.1735
- 943 Hrachowitz, M., Savenije, H., Blöschl, G., McDonnell, J., Sivapalan, M., Pomeroy,
944 J., ... Cudennec, C. (2013). A decade of predictions in ungauged basins
945 (pub)—a review. *Hydrological Sciences Journal*, 58(6), 1198-1255. doi:
946 10.1080/02626667.2013.803183
- 947 Huang, C.-W., Domec, J.-C., Ward, E. J., Duman, T., Manoli, G., Parolari, A. J.,
948 & Katul, G. G. (2017). The effect of plant water storage on water fluxes
949 within the coupled soil-plant system. *New Phytologist*, 213(3), 1093-1106. doi:
950 10.1111/nph.14273
- 951 Jensen, L., Mueller, T., Tate, K., Ross, D., Magid, J., & Nielsen, N. (1996). Soil
952 surface co2 flux as an index of soil respiration in situ: A comparison of two
953 chamber methods. *Soil Biology and Biochemistry*, 28(10), 1297-1306. doi:
954 https://doi.org/10.1016/S0038-0717(96)00136-8
- 955 Jung, M., Reichstein, M., Margolis, H. A., Cescatti, A., Richardson, A. D., Arain,
956 M. A., ... Williams, C. (2011). Global patterns of land-atmosphere fluxes of
957 carbon dioxide, latent heat, and sensible heat derived from eddy covariance,
958 satellite, and meteorological observations. *Journal of Geophysical Research:*
959 *Biogeosciences*, 116(G3). doi: https://doi.org/10.1029/2010JG001566
- 960 Knoben, W. J. M., Freer, J. E., & Woods, R. A. (2019). Technical note: Inher-
961 ent benchmark or not? comparing nash-sutcliffe and kling-gupta efficiency
962 scores. *Hydrology and Earth System Sciences*, 23(10), 4323-4331. doi:
963 10.5194/hess-23-4323-2019
- 964 Kratzert, F., Klotz, D., Brenner, C., Schulz, K., & Herrnegger, M. (2018). Rainfall-
965 runoff modelling using long short-term memory (lstm) networks. *Hydrology and*
966 *Earth System Sciences*, 22(11), 6005-6022. doi: 10.5194/hess-22-6005-2018
- 967 Kratzert, F., Klotz, D., Shalev, G., Klambauer, G., Hochreiter, S., & Nearing, G.
968 (2019). Towards learning universal, regional, and local hydrological behaviors via
969 machine learning applied to large-sample datasets. *Hydrology and Earth System*
970 *Sciences*, 23(12), 5089-5110. doi: 10.5194/hess-23-5089-2019
- 971 Le, P. V. V., Kumar, P., & Drewry, D. T. (2011). Implications for the hydrologic
972 cycle under climate change due to the expansion of bioenergy crops in the
973 midwestern united states. *Proceedings of the National Academy of Sciences*,
974 108(37), 15085-15090. doi: 10.1073/pnas.1107177108
- 975 Leclerc, M. Y., & Foken, T. (2014). *Footprints in micrometeorology and ecology*
976 (Vol. 239). Springer.
- 977 Leroux, L., Bégué, A., Seen, D. L., Jolivot, A., & Kayitakire, F. (2017). Driving forces
978 of recent vegetation changes in the Sahel: Lessons learned from regional and
979 local level analyses. *Remote Sensing of Environment*, 191, 38-54.
- 980 Liang, J., Guo, Q., Zhang, Z., Zhang, M., Tian, P., & Zhang, L. (2020). *Influence*
981 *of complex terrain on near-surface turbulence structures over loess plateau*
982 (Vol. 11) (No. 9). doi: 10.3390/atmos11090930
- 983 Meng, Y., Yang, M., Liu, S., Mou, Y., Peng, C., & Zhou, X. (2021). Quantitative
984 assessment of the importance of bio-physical drivers of land cover change based
985 on a random forest method. *Ecological Informatics*, 61, 101204.
- 986 Meyer, H., Reudenbach, C., Wöllauer, S., & Nauss, T. (2019). Importance of spatial
987 predictor variable selection in machine learning applications—moving from data
988 reproduction to spatial prediction. *Ecological Modelling*, 411, 108815.
- 989 Minns, A. W., & Hall, M. J. (1996). Artificial neural networks as rainfall-
990 runoff models. *Hydrological Sciences Journal*, 41(3), 399-417. doi:
991 10.1080/02626669609491511
- 992 Moffat, A. M., Papale, D., Reichstein, M., Hollinger, D. Y., Richardson, A. D., Barr,

- 993 A. G., ... Stauch, V. J. (2007). Comprehensive comparison of gap-filling
 994 techniques for eddy covariance net carbon fluxes. *Agricultural and Forest*
 995 *Meteorology*, *147*(3), 209-232.
- 996 Moges, E., Ruddell, B. L., Zhang, L., Driscoll, J. M., Norton, P., Perez, F., &
 997 Larsen, L. G. (2022). Hydrobench: Jupyter supported reproducible hydrological
 998 model benchmarking and diagnostic tool. *Frontiers in Earth Science*, *10*. doi:
 999 10.3389/feart.2022.884766
- 1000 Nash, J., & Sutcliffe, J. (1970). River flow forecasting through conceptual models
 1001 part i — a discussion of principles. *Journal of Hydrology*, *10*(3), 282-290. doi:
 1002 [https://doi.org/10.1016/0022-1694\(70\)90255-6](https://doi.org/10.1016/0022-1694(70)90255-6)
- 1003 Nearing, G. S., Mocko, D. M., Peters-Lidard, C. D., Kumar, S. V., & Xia, Y. (2016).
 1004 Benchmarking NLDAS-2 soil moisture and evapotranspiration to separate un-
 1005 certainty contributions. *Journal of Hydrometeorology*(2013), 160113112628008.,
 1006 doi: 10.1175/JHM-D-15-0063.1
- 1007 Nearing, G. S., Ruddell, B. L., Bennett, A. R., Prieto, C., & Gupta, H. V.
 1008 (2020). Does Information Theory Provide a New Paradigm for Earth Sci-
 1009 ence? Hypothesis Testing. *Water Resources Research*, *56*(2), 1–8. doi:
 1010 <https://doi.org/10.1029/2019WR024918>
- 1011 Nearing, G. S., Ruddell, B. L., Clark, M. P., Nijssen, B., & Peters-Lidard, C. (2018).
 1012 Benchmarking and process diagnostics of land models. *Journal of Hydrometeo-*
 1013 *rology*, *19*(11), 1835 - 1852. doi: 10.1175/JHM-D-17-0209.1
- 1014 Ooba, M., Hirano, T., Mogami, J.-I., Hirata, R., & Fujinuma, Y. (2006). Com-
 1015 parisons of gap-filling methods for carbon flux dataset: A combination of a
 1016 genetic algorithm and an artificial neural network. *Ecological Modelling*, *198*(3),
 1017 473-486.
- 1018 Papale, D., Black, T. A., Carvalhais, N., Cescatti, A., Chen, J., Jung, M., ...
 1019 Ráduly, B. (2015). Effect of spatial sampling from european flux tow-
 1020 ers for estimating carbon and water fluxes with artificial neural networks.
 1021 *Journal of Geophysical Research: Biogeosciences*, *120*(10), 1941-1957. doi:
 1022 10.1002/2015JG002997
- 1023 Papale, D., & Valentini, R. (2003). A new assessment of european forests carbon
 1024 exchanges by eddy fluxes and artificial neural network spatialization. *Global*
 1025 *Change Biology*, *9*(4), 525-535. doi: 10.1046/j.1365-2486.2003.00609.x
- 1026 Pastorello, G., Trotta, C., Canfora, E., Chu, H., Christianson, D., Cheah, Y.-W.,
 1027 ... Papale, D. (2020). The FLUXNET2015 dataset and the oneflux pro-
 1028 cessing pipeline for eddy covariance data. *Scientific Data*, *7*(1), 225. doi:
 1029 10.1038/s41597-020-0534-3
- 1030 Prueger, J., & Parkin, T. (2016a). Ameriflux base us-br1 brooks field site 10- ames.
 1031 *AmeriFlux AMP, (Dataset)*. doi: <https://doi.org/10.17190/AMF/1246038>
- 1032 Prueger, J., & Parkin, T. (2016b). Ameriflux base us-br3 brooks field site 11- ames.
 1033 *AmeriFlux AMP, (Dataset)*. doi: <https://doi.org/10.17190/AMF/1246039>
- 1034 Reichstein, M., Camps-Valls, G., Stevens, B., Jung, M., Denzler, J., Carvalhais, N.,
 1035 & Prabhat. (2019). Deep learning and process understanding for data-driven
 1036 Earth system science. *Nature*, *566*(7743). doi: 10.1038/s41586-019-0912-1
- 1037 Reitz, O., Graf, A., Schmidt, M., Ketzler, G., & Leuchner, M. (2021). Upscaling net
 1038 ecosystem exchange over heterogeneous landscapes with machine learning. *Jour-*
 1039 *nal of Geophysical Research: Biogeosciences*, *126*(2), e2020JG005814.
- 1040 Ruddell, B. L., Drewry, D. T., & Nearing, G. S. (2019). Information Theory for
 1041 Model Diagnostics: Structural Error is Indicated by Trade-Off Between Func-
 1042 tional and Predictive Performance. *Water Resources Research*, *55*(8), 6534–6554.
 1043 doi: 10.1029/2018WR023692
- 1044 Ruddell, B. L., & Kumar, P. (2009a). Ecohydrologic process networks: 1. Identifica-
 1045 tion. *Water Resources Research*, *45*(3), 1–23. doi: 10.1029/2008WR007279
- 1046 Ruddell, B. L., & Kumar, P. (2009b). Ecohydrologic process networks: 1. Identifica-
 1047 tion. *Water Resources Research*, *45*(3), 1–22. doi: 10.1029/2008WR007279

- 1048 Runge, J., Bathiany, S., Bollt, E., Camps-Valls, G., Coumou, D., Deyle, E., ...
 1049 Zscheischler, J. (2019). Inferring causation from time series in Earth system sci-
 1050 ences. *Nature Communications*, *10*(1), 2553. doi: 10.1038/s41467-019-10105-3
 1051 Schmidhuber, J. (2015). Deep learning in neural networks: An overview. *Neural Net-*
 1052 *works*, *61*, 85–117. doi: 10.1016/j.neunet.2014.09.003
 1053 Schreiber, T. (2000). Measuring information transfer. *Physical Review Letters*, *85*(2),
 1054 461. doi: 10.1103/PhysRevLett.85.461
 1055 Sendrowski, A., & Passalacqua, P. (2017). Process connectivity in a naturally pro-
 1056 grading river delta. *Water Resources Research*, *53*(3), 1841–1863. doi: 10.1002/
 1057 2016WR019768
 1058 Sendrowski, A., Sadid, K., Meselhe, E., Wagner, W., Mohrig, D., & Passalacqua, P.
 1059 (2018). Transfer entropy as a tool for hydrodynamic model validation. *Entropy*,
 1060 *20*(1). doi: 10.3390/e20010058
 1061 Shannon, C. (1948). A mathematical theory of communication. *The Bell System Tech-*
 1062 *nical Journal*, *196*(4), 519–520. doi: 10.1016/S0016-0032(23)90506-5
 1063 Sivapalan, M. (2003). Prediction in ungauged basins: A grand challenge for theoret-
 1064 ical hydrology. *Hydrological Processes*, *17*, 3163 - 3170. doi: 10.1002/hyp.5155
 1065 Srivastava, N., Hinton, G., Krizhevsky, A., Sutskever, I., & Salakhutdinov, R. (2014).
 1066 Dropout: A simple way to prevent neural networks from overfitting. *J. Mach.*
 1067 *Learn. Res.*, *15*(1), 1929–1958.
 1068 Sutskever, I., Vinyals, O., & Le, Q. V. (2014). *Sequence to sequence learn-*
 1069 *ing with neural networks* (Vol. 27; Z. Ghahramani, M. Welling, C. Cortes,
 1070 N. Lawrence, & K. Weinberger, Eds.). Curran Associates, Inc. doi:
 1071 <https://doi.org/10.48550/arXiv.1409.3215>
 1072 Suyker, A. (2022a). Ameriflux base us-ne1 mead - irrigated continuous maize site.
 1073 *AmeriFlux AMP, (Dataset)*. doi: <https://doi.org/10.17190/AMF/1246084>
 1074 Suyker, A. (2022b). Ameriflux base us-ne2 mead - irrigated maize-soybean rotation
 1075 site. *AmeriFlux AMP, (Dataset)*. doi: <https://doi.org/10.17190/AMF/1246085>
 1076 Suyker, A. (2022c). Ameriflux base us-ne3 mead - rainfed maize-soybean rotation site.
 1077 *AmeriFlux AMP, (Dataset)*. doi: <https://doi.org/10.17190/AMF/1246086>
 1078 Tennant, C., Larsen, L., Bellugi, D., Moges, E., Zhang, L., & Ma, H. (2020). The
 1079 utility of information flow in formulating discharge forecast models: A case
 1080 study from an arid snow-dominated catchment. *Water Resources Research*,
 1081 *56*(8), e2019WR024908. doi: 10.1029/2019WR024908
 1082 Tramontana, G., Migliavacca, M., Jung, M., Reichstein, M., Keenan, T. F., Camps-
 1083 Valls, G., ... Papale, D. (2020). Partitioning net carbon dioxide fluxes into
 1084 photosynthesis and respiration using neural networks. *Global Change Biology*,
 1085 *26*(9), 5235-5253. doi: <https://doi.org/10.1111/gcb.15203>
 1086 Vetter, M., Churkina, G., Jung, M., Reichstein, M., Zaehle, S., Bondeau, A., ...
 1087 Heimann, M. (2008). Analyzing the causes and spatial pattern of the European
 1088 2003 carbon flux anomaly using seven models. *Biogeosciences*, *5*(2), 561–583.
 1089 doi: 10.5194/bg-5-561-2008
 1090 Wang, D., Ricciuto, D., Post, W., & Berry, M. W. (2011). Terrestrial ecosystem car-
 1091 bon modeling. In D. Padua (Ed.), *Encyclopedia of parallel computing* (p. 2034-
 1092 2039). Boston, MA: Springer US. doi: 10.1007/978-0-387-09766-4_395
 1093 Wang, T., Brender, P., Ciais, P., Piao, S., Mahecha, M. D., Chevallier, F., ... Vac-
 1094 cari, F. P. (2012). State-dependent errors in a land surface model across biomes
 1095 inferred from eddy covariance observations on multiple timescales. *Ecological*
 1096 *Modelling*, *246*, 11-25.
 1097 Welchowski, T., Maloney, K. O., Mitchell, R., & Schmid, M. (2022). Techniques to
 1098 improve ecological interpretability of black-box machine learning models. *Jour-*
 1099 *nal of Agricultural, Biological and Environmental Statistics*, *27*(1), 175-197. doi:
 1100 10.1007/s13253-021-00479-7
 1101 Williams, P. L., & Beer, R. D. (2010). Nonnegative decomposition of multivariate
 1102 information. *arXiv preprint arXiv:1004.2515*.

- 1103 Woo, D. K., & Kumar, P. (2017). Role of micro-topographic variability on the distri-
1104 bution of inorganic soil-nitrogen age in intensively managed landscape. *Water*
1105 *Resources Research*, *53*(10), 8404-8422. doi: 10.1002/2017WR021053
- 1106 Xiao, J., Chevallier, F., Gomez, C., Guanter, L., Hicke, J. A., Huete, A. R., ...
1107 Zhang, X. (2019). Remote sensing of the terrestrial carbon cycle: A review of
1108 advances over 50 years. *Remote Sensing of Environment*, *233*, 111383. doi:
1109 <https://doi.org/10.1016/j.rse.2019.111383>
- 1110 Xiao, J., Davis, K. J., Urban, N. M., Keller, K., & Saliendra, N. Z. (2011). Upscaling
1111 carbon fluxes from towers to the regional scale: Influence of parameter vari-
1112 ability and land cover representation on regional flux estimates. *Journal of*
1113 *Geophysical Research: Biogeosciences*, *116*(G3).
- 1114 Xu, M., & Qi, Y. (2001). Soil-surface CO_2 efflux and its spatial and temporal
1115 variations in a young ponderosa pine plantation in Northern California. *Global*
1116 *Change Biology*, *7*(6), 667-677. doi: <https://doi.org/10.1046/j.1354-1013.2001>
1117 .00435.x
- 1118 Yan, Q., Le, P. V. V., Woo, D. K., Hou, T., Filley, T., & Kumar, P. (2019). Three-
1119 dimensional modeling of the coevolution of landscape and soil organic carbon.
1120 *Water Resources Research*, *55*(2), 1218-1241. doi: 10.1029/2018WR023634
- 1121 Zhou, Q., Fellows, A., Flerchinger, G. N., & Flores, A. N. (2019). Examining inter-
1122 actions between and among predictors of net ecosystem exchange: A machine
1123 learning approach in a semi-arid landscape. *Scientific Reports*, *9*(1), 2222. doi:
1124 [10.1038/s41598-019-38639-y](https://doi.org/10.1038/s41598-019-38639-y)
- 1125 Zhou, X., Wang, X., Tong, L., Zhang, H., Lu, F., Zheng, F., ... Ouyang, Z. (2012).
1126 Soil warming effect on net ecosystem exchange of carbon dioxide during the
1127 transition from winter carbon source to spring carbon sink in a temperate
1128 urban lawn. *Journal of Environmental Sciences*, *24*(12), 2104-2112. doi:
1129 [https://doi.org/10.1016/S1001-0742\(11\)61057-7](https://doi.org/10.1016/S1001-0742(11)61057-7)